



# Multiwavelength Observations of Multiple Eruptions of the Recurrent Nova M31N 2008-12a

Judhajeet Basu<sup>1,2</sup>, M. Pavana<sup>1,2</sup>, G. C. Anupama<sup>1</sup>, Sudhanshu Barway<sup>1</sup>, Kulinder Pal Singh<sup>3</sup>, Vishwajeet Swain<sup>4</sup>, Shubham Srivastav<sup>5,6</sup>, Harsh Kumar<sup>4,7,8</sup>, Varun Bhalerao<sup>4</sup>, L. S. Sonith<sup>1,2</sup>, and G. Selvakumar<sup>1</sup>

<sup>1</sup> Indian Institute of Astrophysics, 2nd Block Koramangala, Bangalore 560034, India; [judhajeet20@gmail.com](mailto:judhajeet20@gmail.com)

<sup>2</sup> Pondicherry University, R.V. Nagar, Kalapet, Puducherry 605014, India

<sup>3</sup> Department of Physical Sciences, Indian Institute of Science Education and Research Mohali, Punjab 140306, India

<sup>4</sup> Physics Department, Indian Institute of Technology Bombay, Powai, Mumbai 400076, India

<sup>5</sup> Astrophysics, Department of Physics, University of Oxford, Keble Road, Oxford OX1 3RH, UK

<sup>6</sup> Astrophysics Research Centre, School of Mathematics and Physics, Queen's University Belfast, Belfast BT7 1NN, UK

<sup>7</sup> Harvard College Observatory, Harvard University, 60 Garden Street, Cambridge, MA 02158, USA

<sup>8</sup> Center for Astrophysics, Harvard University, 60 Garden Street, Cambridge, MA 02158, USA

Received 2023 October 9; revised 2024 February 17; accepted 2024 February 19; published 2024 April 24

## Abstract

We report the optical, UV, and soft X-ray observations of the 2017–2022 eruptions of the recurrent nova M31N 2008-12a. We find a *cusp* feature in the  $r'$ - and  $i'$ -band light curves close to the peak, which could be related to jets. The geometry of the nova ejecta based on morpho-kinematic modeling of the  $H\alpha$  emission line indicates an extended jet-like bipolar structure. Spectral modeling indicates an ejecta mass of  $10^{-7}$ – $10^{-8} M_{\odot}$  during each eruption and an enhanced helium abundance. The supersoft source phase shows significant variability, which is anticorrelated to the UV emission, indicating a common origin. The variability could be due to the reformation of the accretion disk. We infer a steady decrease in the accretion rate over the years based on the intereruption recurrence period. A comparison of the accretion rate with different models on the  $M_{\text{WD}}-\dot{M}$  plane yields the mass of a CO white dwarf, powering the *H-shell flashes* every  $\sim 1$  yr, to be  $>1.36 M_{\odot}$  and growing with time, making M31N 2008-12a a strong candidate for the single degenerate scenario of the Type Ia supernovae progenitor.

*Unified Astronomy Thesaurus concepts:* [Recurrent novae \(1366\)](#); [Andromeda Galaxy \(39\)](#); [Cataclysmic variable stars \(203\)](#); [Transient sources \(1851\)](#); [Photometry \(1234\)](#); [Spectroscopy \(1558\)](#); [Ultraviolet astronomy \(1736\)](#); [X-ray astronomy \(1810\)](#)

*Supporting material:* machine-readable tables

## 1. Introduction

Nova eruptions are a consequence of thermonuclear runaway on the surface of a white dwarf (WD) primary in cataclysmic binary systems, resulting in the ejection of material in the range of  $10^{-7}$ – $10^{-4} M_{\odot}$  (Gehrz et al. 1998; Hernanz & Jose 1998; Starrfield 1999). Inherently, all novae are supposed to be recurrent, with the primary WD and the secondary red-giant (RG)/subgiant star sustaining all the eruptions. The observed recurrence period of novae can range from 1 yr (M31N 2008-12a; Darnley et al. 2014) to 98 yr (V2487 Ophiuchi; Schaefer 2010).

M31N 2008-12a is an extraordinary recurrent nova (RN) whose eruptions have been observed every year in 2008–2023 (Table 1). It was first discovered during its 2008 eruption by Nishiyama & Kabashima (2008), although previous eruptions in 1992, 1993, and 2001 have been retrieved from the archives. Since the 2013 eruption, it has been monitored and studied across different wavelength ranges to understand its short recurrence period (2013 eruption—Darnley et al. 2014; Henze et al. 2014a; Tang et al. 2014; 2014—Darnley et al. 2015c; Henze et al. 2015c; 2015—Darnley et al. 2016, 2017b, 2017c; 2016—Henze et al. 2018e).

The optical light curve and spectral evolution of this very fast RN were found to be similar during all the eruptions, with Balmer, He, and N lines dominating the spectrum. Light curves

showed an extremely rapid rise to maximum ( $\sim 1$  day) followed by a fast linear decline for about 4 days and a plateau with slow decline and jitters from day 4 to 8. The multieruption ultraviolet (UV) light curves were similar, with an initial rapid linear decline followed by slow plateau-like declines. The plateau phase coincided with the supersoft X-ray source (SSS) phase. Like optical and UV light curves, the SSS phase was similar during multiple eruptions.

The 2016 eruption (Henze et al. 2018e), however, deviated from the general trend. It occurred after a longer intereruption gap, the optical light curve showed a short-lived cuspy feature, and the UV and X-ray fluxes disappeared relatively early compared to the previous eruptions. The *peculiar* behavior of the 2016 eruption was suggested to be due to a lower accretion rate prior to the 2016 eruption.

Theoretical models generated to satisfy the short recurrence period and short turn-on time of the SSS phase have allowed constraining the mass of the WD to near the Chandrasekhar limit (Kato et al. 2014; Tang et al. 2014).

Deep  $H\alpha$  and Hubble Space Telescope (HST) imaging revealed the presence of an elliptical ( $134 \times 90$  pc) super-remnant nebula around M31N 2008-12a (Darnley et al. 2015c). The size and mass of the shell indicate that the system has been undergoing eruptions for  $\sim 10^6$  yr (Darnley et al. 2019c) and would likely do so for  $\sim 2 \times 10^4$  more years before the WD attains  $M_{\text{Ch}}$  (Darnley et al. 2017c).

This paper discusses the optical photometric and spectroscopic observations during the 2017–2022 eruptions and the evolution of

**Table 1**  
All Known Eruption Dates of M31N 2008-12a till 2023

Eruption Date <sup>a</sup> (UT)	Discovery (mag) (filter)	SSS-on Date <sup>b</sup> (UT)	Days Since Last Eruption	Detection Wavelength (Observatory)	References
(1992 Jan 28)	...	1992 Feb 3	...	X-ray (ROSAT)	(1), (2)
(1993 Jan 3)	...	1993 Jan 9	341	X-ray (ROSAT)	(1), (2)
(2001 Aug 27)	...	2001 Sep 2	...	X-ray (Chandra)	(2), (3)
2008 Dec 25	...	...	...	Visible (Miyaki-Argenteus)	(4)
2009 Dec 2	...	...	342	Visible (Palomar Transient Factory (PTF))	(5)
2010 Nov 19	...	...	352	Visible (Miyaki-Argenteus)	(2)
2011 Oct 22.5	...	...	337.5	Visible (ISON-New Mexico)	(5)–(8)
2012 Oct 18.7	...	<2012 Nov 6.45	362.2	Visible (Miyaki-Argenteus)	(8)–(11)
2013 Nov 26.95 ± 0.25	18.9 ( <i>R</i> )	≤2013 Dec 3.03	403.5	Visible (iPTF); UV/X-ray (Swift)	(5), (8), (11)–(14)
2014 Oct 2.69 ± 0.21	18.86 ( <i>r'</i> )	2014 Oct 8.6 ± 0.5	309.8 ± 0.7	Visible (Liverpool Telescope (LT)); UV/X-ray (Swift)	(8), (15)
2015 Aug 28.28 ± 0.12	19.09 ( <i>r'</i> )	2015 Sep 2.9 ± 0.7	329.6 ± 0.3	Visible (Las Cumbres Observatory (LCO)); UV/X-ray (Swift)	(14), (16)–(18)
2016 Dec 12.32 ± 0.17	17.62 ( <i>V</i> )	2016 Dec 17.2 ± 1.1	471.7 ± 0.2	Visible (Itagaki); UV/X-ray (Swift)	(19)–(23)
2017 Dec 31.58 ± 0.20 <sup>c</sup>	18.41 (clear)	2018 Jan 5.6 ± 0.5	384.3 ± 0.4	Visible (West Challow Observatory); UV/X-ray (Swift)	(24)–(27)
2018 Nov 6.67 ± 0.13 <sup>c</sup>	19.15	2018 Nov 13.2 ± 0.5	310.1 ± 0.3	Visible (LT); UV/X-ray (Swift)	(28)–(31)
2019 Nov 6.60 ± 0.11 <sup>c</sup>	19.40	2019 Nov 12.4 ± 0.5	364.9 ± 0.2	Visible (Hankasalmi Observatory); UV/X-ray (Swift)	(32)–(34)
2020 Oct 30.49 ± 0.34 <sup>c</sup>	18.74 ( <i>g'</i> )	2020 Nov 5.5 ± 0.9	358.9 ± 0.4	Visible (LT); UV/X-ray (Swift)	(35)–(38)
2021 Nov 14.17 ± 0.21 <sup>c</sup>	18.7 (clear)	2021 Nov 19.2 ± 0.6	379.7 ± 0.5	Visible (Itagaki); UV/X-ray (Swift)	(39)–(42)
2022 Dec 2.50 ± 0.34 <sup>c</sup>	19.18 ( <i>r'</i> )	2022 Dec 7.5 ± 0.5	383.3 ± 0.5	Visible (LCOGT); UV/X-ray (Swift)	(43)–(45)
2023 Dec 5.28 ± 0.07 <sup>c,d</sup>	18.63 (CV)	...	367.8 ± 0.4	Visible (Half Meter Telescope, Xingming Observatory)	(46)–(50)

**Notes.** Updated version of Table 1 of Tang et al. (2014), Darnley et al. (2015c, 2016), and Henze et al. (2015a, 2018e). ... indicates unavailability of information.

<sup>a</sup> Archival X-ray detections (see Henze et al. 2015a) are enclosed in brackets.

<sup>b</sup> ROSAT data were used to estimate the SSS  $t_{\text{on}}$  for 1992 and 1993. The Chandra detection in 2001 September 8 UT was taken as the midpoint of a typical 12 days SSS phase to constrain the eruption date.

<sup>c</sup> Determined in this paper.

<sup>d</sup> The 2023 eruption was discovered during the revision of the manuscript. As the observations are still ongoing, all details are not yet available.

**References.** (1) White et al. (1995), (2) Henze et al. (2015a), (3) Williams et al. (2004), (4) Nishiyama & Kabashima (2008), (5) Tang et al. (2014), (6) Korotkiy & Elenin (2011), (7) Barsukova et al. (2011), (8) Darnley et al. (2015c), (9) Nishiyama & Kabashima (2012), (10) Shafter et al. (2012), (11) Henze et al. (2014a), (12) Tang et al. (2013), (13) Darnley et al. (2014), (14) Darnley et al. (2016), (15) Henze et al. (2015c), (16) Darnley et al. (2015a), (17) Darnley et al. (2015b), (18) Henze et al. (2015b), (19) Henze et al. (2018e), (20) K. (2016), (21) Itagaki et al. (2016), (22) Henze et al. (2016a), (23) Henze et al. (2016b), (24) Boyd et al. (2017), (25) Henze et al. (2018b), (26) Henze et al. (2018c), (27) Naito et al. (2018), (28) Henze et al. (2018a), (29) Darnley et al. (2018b), (30) Tan & Gao (2018), (31) Henze et al. (2018d), (32) Darnley et al. (2019a), (33) Oksanen et al. (2019), (34) Darnley et al. (2019b), (35) Galloway et al. (2020), (36) Darnley et al. (2020b), (37) Darnley & Page (2020), (38) Darnley et al. (2020a), (39) Itagaki et al. (2021), (40) Tan et al. (2021), (41) Darnley & Pag (2021a), (42) Darnley & Pag (2021b), (43) Perez-Fourmon et al. (2022), (44) Shafter et al. (2022), (45) Darnley et al. (2022), (46) Sun et al. (2023), (47) Shafter et al. (2023), (48) Perez-Fourmon et al. (2023), (49) Basu et al. (2023), (50) Balcon (2023).

UV and soft X-ray emission based on Swift archival data and data from our observations with the AstroSat. We explore spectroscopic modeling to reveal physical processes during outbursts and derive associated physical parameters. The behavior of the RN M31N 2008-12a during the 2017–2022 eruptions is also compared to that of the previous eruptions. We end with a discussion on the recurrence period and its implication on the accretion rate and the mass of the primary WD.

## 2. Observations

### 2.1. Optical

Photometric and spectroscopic observations were carried out using the following telescopes and instruments. The log of optical observations is given in Table 2.

#### 2.1.1. GROWTH-India Telescope

The GROWTH-India Telescope (GIT; Kumar et al. 2022)<sup>9</sup> is a 0.7 m fully robotic telescope at the Indian Astronomical Observatory (IAO), Hanle, India. The telescope has a 4096 × 4108 Andor iKon-XL CCD. The detector has an image scale of 0.67 pixel<sup>-1</sup> with a field of view (FoV) of 0.7°.

The GIT images were preprocessed, i.e., bias subtracted, flat-fielded, and cosmic-ray corrected by the automated pipeline of the GIT (Kumar et al. 2022). Multiple exposures were obtained every night, and in the case of low signal-to-noise ratio (S/N), images from the same night and the same filter were stacked using SWarp (Bertin et al. 2002).

<sup>9</sup> <https://sites.google.com/view/growthindia/about>

**Table 2**  
Optical Spectroscopic and Photometric Observations of 2018–2022 Eruptions of M31N 2008-12a

Date (UT)	Telescope	Instrument	Grating	Exp (s)
2018 Nov 7.8	HCT	HFOSC	Gr7	2700
2018 Nov 8.6	HCT	HFOSC	Gr7	3600
2019 Nov 7.5	HCT	HFOSC	Gr7	3000
2020 Oct 31.6	HCT	HFOSC	Gr7	3600
2021 Nov 14.8	HCT	HFOSC	Gr7	2100
2021 Nov 15.6	HCT	HFOSC	Gr7	3600
2022 Dec 3.7	HCT	HFOSC	Gr7	3600
2022 Dec 4.5	HCT	HFOSC	Gr7	3600

Date (UT)	Telescope	Filter	Magnitude	Exp (s)
2018 Nov 7.58	JCBT	<i>B</i>	19.29 ± 0.28	1800
2018 Nov 7.57	JCBT	<i>V</i>	18.78 ± 0.10	1200
2018 Nov 8.57	HCT	<i>V</i>	19.27 ± 0.13	300 × 3
2018 Nov 8.56	HCT	<i>R</i>	19.11 ± 0.11	180 × 3
2018 Nov 8.55	HCT	<i>I</i>	18.83 ± 0.20	150 × 3
2018 Nov 8.76	GIT	<i>g'</i>	19.60 ± 0.10	300 × 3
2018 Nov 8.77	GIT	<i>r'</i>	19.15 ± 0.09	300 × 3
2018 Nov 8.74	GIT	<i>i'</i>	19.28 ± 0.15	300 × 3

**Note.** The full table of the photometric data will be made available in machine-readable format. The spectroscopic data are not included in the machine-readable table.

(This table is available in its entirety in machine-readable form.)

For the 2018 data, aperture photometry was performed using an aperture of  $\sim 2''.5$ , close to the full width at half-maximum (FWHM) of the stellar profile in the images due to low S/N. For 2020–2022 data, the FWHM was first calculated using SExtractor (Bertin & Arnouts 1996) and subsequently used in Image Reduction and Analysis Facility (IRAF<sup>10</sup>; Tody 1993) to perform point-spread function (PSF) photometry. The magnitudes of the local standard stars given in Darnley et al. (2016) were converted from *BVRI* to *gri* using the transformations in Jester et al. (2005) to determine the zero-points for photometric calibrations. Aperture photometry was also performed and found to be consistent with PSF photometry, eliminating any systematic differences that could arise from aperture photometry of the 2018 data.

### 2.1.2. Himalayan Chandra Telescope

The Himalayan Faint Object Spectrograph Camera (HFOSC)<sup>11</sup> mounted on the 2 m Himalayan Chandra Telescope (HCT) located at IAO, Hanle, India was used to obtain images in the *VRI* bands on 2018 November 8 UT. HFOSC is equipped with a  $2 \times 4K$  CCD. The pixels correspond to an image scale of  $0''.296 \text{ pixel}^{-1}$ , with an FoV of  $10' \times 10'$  for the central  $2 \times 2K$  region. The images were preprocessed using the standard routines in IRAF. The instrumental magnitudes were obtained using aperture photometry with an aperture set at a radius 3 times the FWHM. Differential photometry was

<sup>10</sup> IRAF is distributed by the National Optical Astronomy Observatories, which are operated by the Association of Universities for Research in Astronomy, Inc., under cooperative agreement with the National Science Foundation.

<sup>11</sup> [https://www.iiap.res.in/?q=iao\\_2m\\_hfosc](https://www.iiap.res.in/?q=iao_2m_hfosc)

performed with respect to the local standards (Darnley et al. 2016) to account for the zero-points of the images.

Optical spectra obtained using HFOSC (Pavana et al. 2018; Sonith et al. 2021; Basu et al. 2022) are given in Table 2. We used a grism with  $R \approx 1200$  in the wavelength range of 3500–7800 Å. Data reduction was performed in the standard manner using IRAF. All the spectra were bias subtracted, and cosmic rays were corrected before extraction. Wavelength calibration was carried out using the FeAr arc lamp spectrum. Spectrophotometric standard stars, Feige 110 (2018, 2019, and 2020 eruptions) and Feige 34 (2021 and 2022 eruptions), were used to correct for the instrumental response and bring the spectra to a relative flux scale. The absolute flux calibration was done using the zero-points obtained from broadband magnitudes based on photometric observations within 3–4 hr of the spectroscopic observation, except in the case of the 2020 observations, which had a gap of around 7 hr.

### 2.1.3. J.C. Bhattacharyya Telescope

The  $2 \times 4K$  UK Astronomy Technology Centre CCD mounted on the 1.3 m Jagadish Chandra Bhattacharyya Telescope (JCBT)<sup>12</sup> located at the Vainu Bappu Observatory (VBO), Kavalur, India, was used during the 2018 eruption. It has a  $15 \mu\text{m}$  pixel size corresponding to an image scale of  $0''.3 \text{ pixel}^{-1}$ , with an FoV of  $10' \times 20'$ . JCBT observed the nova in *BV* bands 2 days after the eruption. The images were reduced and calibrated following the same steps used for HCT data.

### 2.1.4. Other Data Sources

Our observations were combined with publicly available photometric data for analysis, from the sources referenced below:

- 2017: Socia et al. (2018), Hornoch et al. (2018), Kaur et al. (2018a, 2018b, 2018c), Naito et al. (2018), Erdman et al. (2018), and Darnley et al. (2018a);
- 2018: Engesser et al. (2018), Agnihotri & Raj (2018a, 2018b), Wysocki et al. (2018), Tan & Gao (2018), and Kaur et al. (2018d); Zwicky Transient Facility (ZTF) archive (ALeRCE Explorer,<sup>13</sup> Förster et al. 2021);
- 2019: Hornoch et al. (2019), Horst et al. (2019), and Kaur et al. (2019); ZTF archive;
- 2020: Perez-Fournon et al. (2020), Galloway et al. (2020), and Rajagopal et al. (2020);
- 2021: Taguchi et al. (2021), Naito et al. (2021);
- 2022: Rodriguez et al. (2023), Shafter et al. (2022), Agnihotri et al. (2022), Tan et al. (2022), and Erdman et al. (2022).

## 2.2. Ultraviolet

Photometric studies were done using images obtained in the UV bands from the following two telescopes.

### 2.2.1. Swift UVOT

High-cadence UV imaging data of M31N 2008-12a are available from the Swift (Gehrels et al. 2004) archive.<sup>14</sup> The nova has been monitored by UVOT since 2013 during each

<sup>12</sup> [https://www.iiap.res.in/?q=centers/vbo#Telescopes\\_VBO](https://www.iiap.res.in/?q=centers/vbo#Telescopes_VBO)

<sup>13</sup> <https://alerce.online/>

<sup>14</sup> <https://www.swift.ac.uk/index.php>

**Table 3**  
AstroSat (UVIT and SXT) and Swift (UVOT and XRT) Observations of 2017–2022 Eruptions of the M31N 2008-12a

AstroSat ObsID	Date (UT)	UVIT F148W (AB mag)	Exp (s)	Count Rate SXT (0.3–2.0) keV ( $\times 10^{-3}$ count s $^{-1}$ )	Exp (s)
T03_156T01_9000003312	2019-11-19.78	23.03 $\pm$ 0.14	8548	...	...
T03_259T01_9000003972	2020-11-03.25	21.30 $\pm$ 0.09	4888	...	...
T03_262T01_9000003988	2020-11-10.76	22.78 $\pm$ 0.12	8170	25.81 $\pm$ 2.18	8909
...	2020-11-11.09	...	...	34.33 $\pm$ 2.68	7254
...	2020-11-11.42	...	...	31.30 $\pm$ 2.18	11355
...	2020-11-11.75	...	...	32.03 $\pm$ 2.52	8215
...	2020-11-12.09	...	...	32.94 $\pm$ 2.22	10178
...	2020-11-12.42	...	...	32.11 $\pm$ 2.14	11358
...	2020-11-12.75	...	...	45.70 $\pm$ 17.31	259
T04_066T01_9000004772	2021-11-18.97	21.25 $\pm$ 0.12	2988	...	...
T04_072T01_9000004780	2021-11-23.22	22.96 $\pm$ 0.09	25,506	23.63 $\pm$ 3.06	4556
...	2021-11-23.41	...	...	31.22 $\pm$ 2.31	8985
...	2021-11-23.74	...	...	26.20 $\pm$ 2.35	7802
...	2021-11-24.07	...	...	31.83 $\pm$ 3.27	4363
...	2021-11-24.41	...	...	31.79 $\pm$ 2.36	9323
...	2021-11-24.74	...	...	34.09 $\pm$ 2.72	7314
...	2021-11-25.07	...	...	24.02 $\pm$ 3.39	3863
...	2021-11-25.41	...	...	25.80 $\pm$ 2.39	8201
...	2021-11-25.74	...	...	33.51 $\pm$ 4.41	2637
T05_058T01_9000005414	2022-12-07.23	21.38 $\pm$ 0.07	7872	...	...

Swift ObsID	Date (UT)	UVOT <i>uvw2</i> (AB mag)	Exp (s)	Count Rate XRT (0.3–1.5) keV ( $\times 10^{-3}$ count s $^{-1}$ )	Exp (s)
00010498001	2018-01-01.22	18.87 $\pm$ 0.05	575	<39.4	986
00010498002	2018-01-02.36	19.59 $\pm$ 0.06	979	<38.1	991
00010498003	2018-01-03.81	20.76 $\pm$ 0.16	754	<55.9	682
00010498004	2018-01-04.49	20.27 $\pm$ 0.09	1249	<30.2	1266
00010498005	2018-01-05.48	20.69 $\pm$ 0.06	1021	3.6 $\pm$ 1.0	5197
00010498006	2018-01-05.94	20.90 $\pm$ 0.07	937	11.8 $\pm$ 1.6	5317
00010498007	2018-01-07.14	21.10 $\pm$ 0.08	1614	12.1 $\pm$ 1.7	5202
00010498008	2018-01-08.07	21.00 $\pm$ 0.08	1637	13.8 $\pm$ 2.0	4155

**Note.** Observation ID (ObsID).

(This table is available in its entirety in machine-readable form.)

eruption. The log of Swift observations between 2017 and 2022 is summarized in Table 3. We have used the *uvw2* (1928  $\pm$  657 Å) archival data in this study. The *uvot* task in HEASOFT (v6.29) was used to extract the magnitudes from a source region of radius 5'' after background subtraction. Since the field is crowded in *uvw2* filter, a source-free 10'' radius circle, 80'' southwards of the object, was chosen to estimate the background. The calibration assumes the UVOT photometric (AB) system (Poole et al. 2008 and Breeveld et al. 2011) and is not corrected for extinction.

### 2.2.2. AstroSat UVIT

AstroSat (Singh et al. 2014) is a space-based telescope with the Ultraviolet Imaging Telescope (UVIT) as one of its instruments. UVIT observed M31N 2008-12a during its 2019–2022 eruptions in F148W (1481  $\pm$  500 Å) filter (see Table 3). The level 1 UVIT data were downloaded from the Indian Space Science Data Center (ISSDC)<sup>15</sup> and reduced using CCDLAB following standard routines presented in Postma & Leahy (2021). The orbit-wise images were registered and merged to obtain a single image with a high S/N on which astrometry was performed. The average PSF size in UVIT

images was  $\sim 1''.5$  across all epochs. We performed PSF photometry with an aperture correction term derived from *good stars* to account for the broad PSF wings in UVIT images. The zero-points for photometric calibrations in the AB system were adopted from Tandon et al. (2020) and have not been corrected for extinction.

### 2.3. X-Ray

Both Swift and AstroSat observe simultaneously in the UV and X-ray wavelengths. Soft X-ray observations from both facilities were used to study the eruptions during the SSS phase.

#### 2.3.1. Swift XRT

Swift X-Ray Telescope (XRT; Burrows et al. 2005) data were downloaded from the Swift archive, with the Observation IDs being same as that of the UVOT data (Table 3). For the analysis, HEASOFT (v6.29) with XIMAGE (v4.5.1) and XSELECT (v2.5b) were used following the guidelines summarized by UKSSDC.<sup>16</sup> XRT count rates were determined using both XIMAGE and XSELECT tools provided by HEASARC. Both results followed the same trend and were within 1 $\sigma$  errors of each other. We have presented the results

<sup>15</sup> [https://astrobrowse.issdc.gov.in/astro\\_archive/archive/Home.jsp](https://astrobrowse.issdc.gov.in/astro_archive/archive/Home.jsp)

<sup>16</sup> <https://www.swift.ac.uk/analysis/>



from the XIMAGE *sosta/optimize* analysis as it corrects the counts for vignetting, dead time loss, background subtraction, and the PSF of the instrument. We used XSELECT to extract the spectra for each snapshot. Ancillary Response Files (ARF) files were generated from the exposure maps, while Response Matrix Files files were taken from the calibration database. Spectral analysis was performed in XSPEC (v12.12.0) assuming Poisson statistics (*cstat*) due to low counts. We used interstellar medium (ISM) abundances given in Wilms et al. (2000) and the Tübingen-Boulder (*tbabs*) ISM absorption model to account for the intervening medium.

### 2.3.2. AstroSat SXT

AstroSat soft X-ray telescope (SXT; Singh et al. 2017), placed in parallel alongside UVIT, is capable of observing in the 0.3–8.0 keV range simultaneously with UVIT (Table 3). SXT observed the SSS phase of M31N 2008-12a during the 2020 and 2021 eruptions. Level 2 data were downloaded from ISSDC, and the cleaned event files were merged using SXTTools in Julia.<sup>17</sup> The source region was chosen as a circle of radius 7', smaller than the usual SXT PSF of  $\sim 12'$  so to avoid contamination in the crowded M31 field. We set the bin size to 8 hr and energy range to 0.3–2.0 keV in XSELECT (XIMAGE was avoided due to compatibility issues) to attain an adequate S/N for light-curve analysis. SXT spectra were extracted using XSPEC from the merged SXT cleaned event files. A new ARF file was generated corresponding to the smaller source extraction region for analysis.

### 2.4. Epoch of Eruptions

For a very fast RN, like M31N 2008-12a, a tight constraint on the eruption time is useful for generating light-curve models (Section 3.3) and studying its recurrence nature (Section 7). Hence, we estimate the epochs of eruption based on available detection and pre-discovery magnitudes, and the nondetection upper limits for all eruptions since 2017. Even though the exact time of eruption is uncertain, it can be well approximated by the mid-point of first detection and last nondetection in each year. Amateur astronomers' interest in M31 and the increase in survey telescopes over the past decade have made it possible to constrain the eruption date to well within a day. The uncertainty in the eruption dates spans between the first detection and the last nondetection.

The 2017 eruption was discovered just in time to be called the “2017 eruption” on December 31.77 UT by Boyd et al. (2017). Darnley et al. (2017a) reported spectroscopic confirmations on the same day. The last nondetection was on December 31.38 UT at an upper limit of  $m_{\text{clear}} = 19$  mag (Naito et al. 2018).

The 2018 eruption was discovered on November 6.80 UT at a magnitude of  $19.15 \pm 0.05$  by Darnley et al. (2018b) and confirmed spectroscopically by Darnley et al. (2018c) on the same day. Tan & Gao (2018) reported the last nondetection at  $>21.20$  mag on November 6.54 UT in a clear filter.

The 2019 eruption was detected on November 6.71 UT by Oksanen et al. (2019) at 19.40 mag. The first spectrum taken on November 6.83 UT (Darnley et al. 2019d) confirmed the recurrence of M31N 2008-12a. The last nondetection

information was not publicly available for 2019, so we adopted the eruption date provided in Darnley et al. (2019b).

Darnley et al. (2020b) discovered the 2020 eruption on October 30.89 UT. The nova was, however, also detected in images captured 90 minutes before the discovery (Galloway et al. 2020), and we use the pre-discovery detection ( $m_g = 18.74$ ) and nondetection ( $m_g > 19.4$ ) to constrain the eruption time. The discovery was spectroscopically confirmed on the next day (Darnley 2020).

The 2021 eruption was discovered on November 14.38 UT by Itagaki et al. (2021) and was spectroscopically confirmed by Wagner et al. (2021). Tan et al. (2021) gave pre-detection upper-limits at  $m_{\text{clear}} > 19.00$  mag on November 13.96 UT.

The 2022 eruption was discovered on December 2.83 UT by Perez-Fournon et al. (2022). It was undetected until December 2.61 UT at  $m_L > 19.60$  mag (Shafter et al. 2022). Spectra taken on December 3.84 UT confirmed the source to be a recurrence of the nova (Darnley & Healy 2022), its 15th successive eruption in as many years.

The estimated eruption dates for 2017–2023 are presented in Table 1 together with those of the previous ones.

## 3. UV and Optical Light Curve

### 3.1. Light-curve Evolution

The optical light curves of the 2017–2022 eruptions, based on our observations and publicly available data, are shown in Figure 1. The light curves indicate a rapid rise to the peak magnitude in  $<1$  day from discovery, followed by a fast decline with  $t_2 \approx 2$ –4 days in  $g'r'i'$  bands. A brief description of the optical light curve for each eruption during 2017–2022 is provided below.

The 2017 light curves show a rapid decline in the first 4 days, followed by a slow decline in all the bands. The decline rate is marginally faster in the  $r'$  band ( $0.84 \pm 0.12$  mag day<sup>-1</sup>) compared to the  $g'$  band ( $0.74 \pm 0.19$  mag day<sup>-1</sup>). However, the decline rates in  $g'$  and  $r'$  were measured using only two data points and are within error bars of each other.

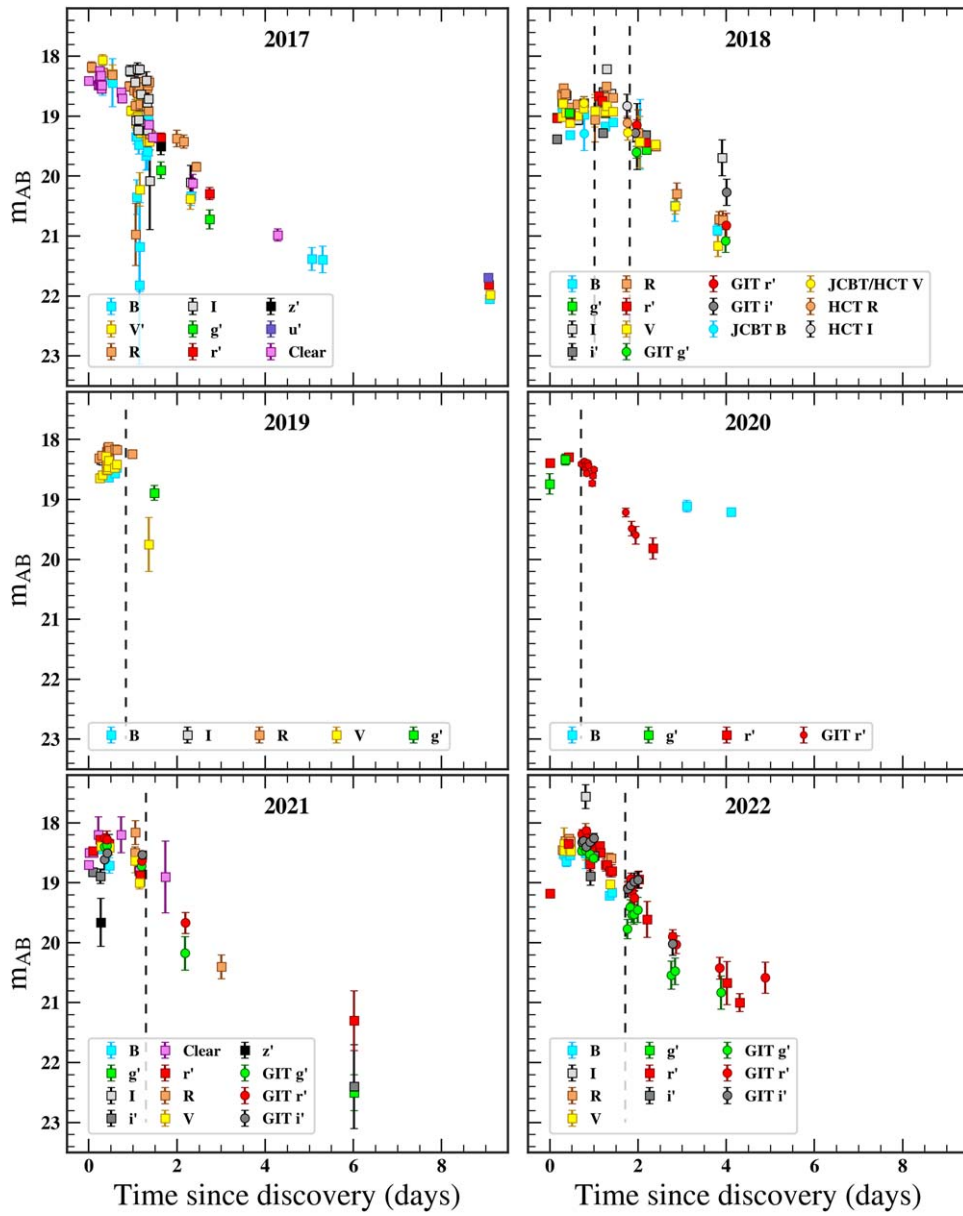
The maximum phase during the 2018 eruption appears to be broader. Following the initial rise, the magnitude declined by  $\sim 0.4$  mag in the *BVRI* filters, and after a brief halt for about 0.3 day at this level, a marginal increase in the brightness by 0.2–0.3 mag lasting  $\sim 0.7$  day can be seen. We also note that the peak magnitude observed in 2018 in  $R$  (18.50 mag) is fainter than the peak  $R$  or  $r$  magnitudes in the other years. In 2018, the initial decline in the  $r'$  ( $0.68 \pm 0.03$  mag day<sup>-1</sup>) and  $i'$  ( $0.53 \pm 0.04$  mag day<sup>-1</sup>) bands was slower by 0.1–0.2 mag day<sup>-1</sup> compared to other years. Further, the decline rates of  $r'$  and  $i'$  are slower than  $g'$  band ( $0.84 \pm 0.02$  mag day<sup>-1</sup>) in 2018.

The 2019 data set is sparse and restricted to the initial rise and maximum phases. The nova is brighter in  $R$  compared to *BV* bands during the rise and the peak. It rises about 0.4 mag in all the bands in about 0.5 day from discovery. The peak  $R$  magnitude reached in 2019 is  $m_R = 18.12$ , which is higher than most other eruptions.

The  $g'$  band traces the rise of the 2020 light curve at  $\sim 1.2$  mag day<sup>-1</sup> while the  $r'$  band traces the smooth decline from the peak at  $0.89 \pm 0.05$  mag day<sup>-1</sup> for 2 days. Limited data only restricts the light-curve analysis to the  $r'$  band.

The 2021 eruption was caught almost a day before it reached its peak. The rise was sharper in the  $i'$  band compared to the  $g'r'$  bands. It declined rapidly in the  $g'$  band at  $1.25 \pm 0.20$  mag day<sup>-1</sup>

<sup>17</sup> <http://astrosat-ssc.iucaa.in/sxtData>



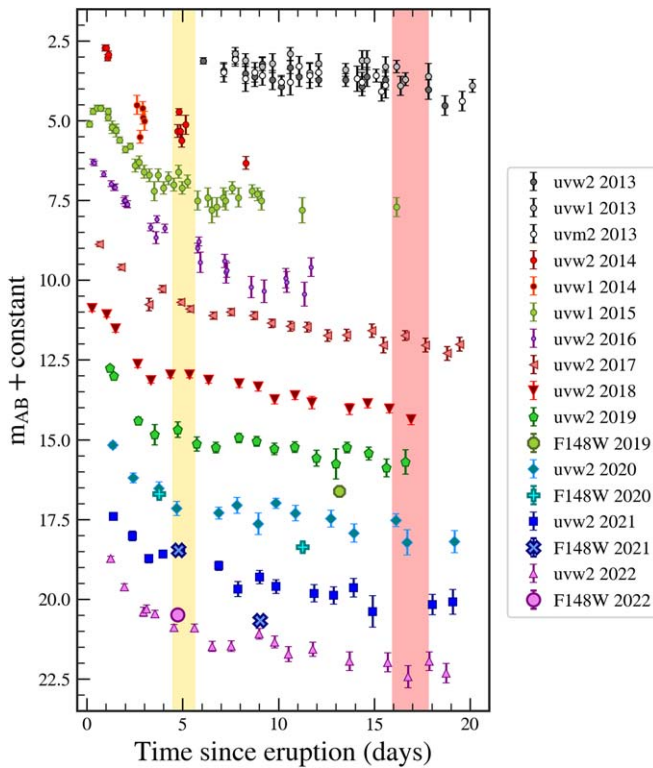
**Figure 1.** Optical light curves of M31N 0808-12a for 2017–2022 eruptions. GIT, HCT, and JCBT observations are plotted with publicly available data. Vertical dashed lines in each panel mark the epochs of spectroscopic observations.

but relatively slowly in the  $r'$  band at  $0.88 \pm 0.13 \text{ mag day}^{-1}$  for the first 3–4 days. The decline rate then slowed with significant enhancement in the  $r'$ -band flux around 6 days after the eruption.

The 2022 eruption light curve was similar to previous years. The rise is well captured in the  $r'$  band with a rate of  $\sim 2 \text{ mag day}^{-1}$ , the fastest in the last 6 yr. It then declined speedily in the  $g'$  band ( $1.01 \pm 0.05 \text{ mag day}^{-1}$ ) but relatively slowly in  $r'$  band ( $0.79 \pm 0.03 \text{ mag day}^{-1}$ ) and even more slowly in the  $i'$  band ( $0.69 \pm 0.06 \text{ mag day}^{-1}$ ).

Generally, the nova declines fastest in the  $g'$  band and comparatively slower in the redder bands. Darnley et al. (2016) combined the 2013, 2014, and 2015 eruptions and found the decline rate to be fastest in the  $V$  band at  $1.21 \text{ mag day}^{-1}$  during the initial decline phase. The evolution of the optical light curve during the later phases is unavailable as the nova fades beyond the detection limit of the 1–2 m class ground-based telescopes generally used for follow-up observations.

The UV light curves (Figure 2) obtained from space-based telescopes have a wider time coverage ( $\sim 20$  days) and show a linear decline in the 2017–2022  $uvw2$  magnitudes from day 0 to 3 since the eruption. The plateau phase begins with a rebrightening at  $\sim 4$  days since the eruption, which is also coincident with the SSS turn-on time (yellow shaded region in Figure 2). The evolution during this phase indicates a gradual decline of  $\sim 0.15 \text{ mag day}^{-1}$ . However, this decline is not smooth but accompanied by small undulations. Some P-type galactic recurrent novae, such as T Pyx, RS Oph, and U Sco, show variability in the  $V$  band during their plateau phase (Strope et al. 2010). Since the optical photometry during this phase is insufficient, we are unable to comment on the presence of a similar variability in the optical bands in the case of M31 0808-12a. We encourage continuous and deep optical monitoring during the plateau phase in future eruptions.



**Figure 2.** UVOT light curves of M31N 2008-12a shown for 2013–2022 eruptions. UVIT F148W data are overplotted. SSS  $t_{\text{on}}$  and  $t_{\text{off}}$  times are highlighted in yellow and red respectively.

The F148W data indicate a brightness similar to  $uvw2$  during the initial decline phase, but becomes fainter than  $uvw2$  by  $>0.5$  mag during the SSS phase.

The general trends across all the UV–optical bands in 2017–2022 eruptions are more or less similar over the last 6 yr and consistent with the previous eruptions (2013, Darnley et al. 2014; 2014, Darnley et al. 2015c; 2015, Darnley et al. 2016; 2016, Henze et al. 2018e). However, some deviations of the 2016 light curve were noted and are discussed in Section 8.

### 3.2. Color Evolution

The  $(F148W - uvw2)$  color was determined from observations taken on the same day. From Figure 3, it is seen that the  $(F148W - uvw2)$  color becomes bluer at the onset of the SSS phase but is significantly redder during the SSS phase.

In the optical bands, we restrict the color analysis to only the SDSS primed filters to avoid instrumental and/or filter dependencies of the Bessel filters. Near-simultaneous observations in  $g'r'$  and  $r'i'$  filters for the same eruption were used to estimate the colors. The colors are plotted together as a function of days since the eruption to bring all the outbursts to the same timescale. The  $(g' - r')$  color linearly increases up to day 3 from the eruption and then decreases. This timeline agrees with the initial rise and linear decline phase of the light curve. The  $(r' - i')$  color shows a steep reddening during the rising phase, which then slows down as the nova follows its initial decline. After 3 days from the eruption, the  $(g' - r')$  color becomes bluer while the  $(r' - i')$  color also tends to be bluer, but due to only one data point between day 3 and day 4, we are unable to confirm this. Beyond day 4, the  $(r' - i')$  color becomes redder

when the nova enters its plateau phase. A similar trend was also noted by Darnley et al. (2016) in their color plots.

### 3.3. Light-curve Modeling

To understand the temporal evolution of the light curves, we model them by breaking them into three phases corresponding to different decline rates. The  $uvw2$ ,  $g'$ ,  $r'$ , and  $i'$  bands are used. The eruption times presented in Table 1 are used as the reference times, and we measure all other times in *days* with respect to the reference date of each eruption. The three phases considered are

1. the rise to peak, from eruption to  $t \approx 1.5$ ;
2. the initial steep decline,  $t_{\text{max}} \leq t \leq 3.5$ , where  $t_{\text{max}}$  is the time of maxima;
3. the slow decline,  $t \geq 3.5$ .

Due to extensive coverage in the  $uvw2$  filter, we could notice that the rate of decline decreased even further beyond 8 days of eruption. The final phase is thus divided into two segments in  $uvw2$ . Darnley et al. (2016) employed a similar four-phase division of all light curves to analyze previous eruptions.

First, we generated models for the combined 2017–2022 eruptions and obtained the light-curve properties at different phases given in Table 4. Then, we combined the 2013–2015 eruptions’ data (see Section 1 for references) with those from 2017 to 2022 and generated overall light-curve models spanning from 2013 to 2022. We note here that the data in  $g'$  are sparse as it was not used in most of the observations before 2016. The 2016 data set has been intentionally excluded as an outlier as it deviated significantly from the general trend of other eruptions (plotted in red points in Figure 4), especially in the UV light curve. The combined light-curve models are presented in Figure 4, and the light-curve parameters are tabulated in Table 4.

Additionally, Gaussian process regression (GPR) techniques were employed to fit the entire light curve for each band. The regression results, including a  $3\sigma$  error range, are shown in blue in Figure 4.

#### 3.3.1. The Rise to Peak

This phase has been modeled with a quadratic function to trace the rise to the peak and the fall just after. The limited availability of  $uvw2$  data during this phase led to only partial modeling of the rise in this band. On the other hand, the optical bands have dense coverage of the rise and the peak. The  $uvw2$  and  $g'$  bands show a smooth rise toward the peak and a smooth decline from the peak. In contrast, the  $r'$  and  $i'$  bands show a *cusp* just before the peak of the modeled light curve is attained.

On combining the 2013–2015 light curves with those from 2017 to 2022, we clearly see the cusp (Figure 4), at least in  $r'$  and  $i'$  bands, just before the peak is attained. The cusp-like feature is evident in the 2021 and 2022 light curves (Figure 1) as the data points are dense. The 2018 light curve also indicates the presence of the cusp, although with lesser brightness. The 2017  $V$ -band and 2019  $R$ -band data also hint at the cusp. Observations post-2016 indicate that the cusp is most likely present during all eruptions. The cusp was first noted by Henze et al. (2018e) in the 2016 eruption in multiple wave bands, who speculated the “cusp” could be an isolated event in 2016 (and 2010?), connected to the short SSS phase and long

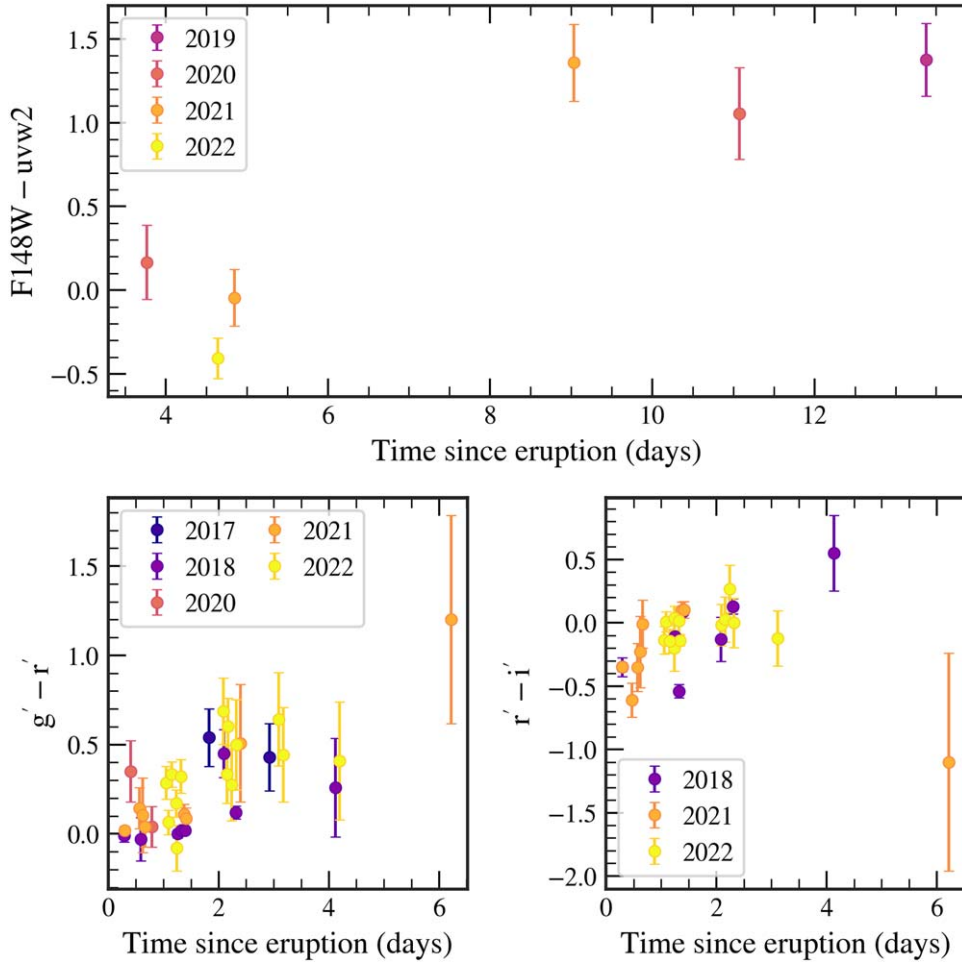


Figure 3. Color evolution of M31N 2008-12a in UV and optical bands for 2017–2022 eruptions.

intereruption period of the 2016 event. Alternatively, as indicated by Henze et al. (2018e), and Darnley & Henze (2020), the low-cadence observations of the 2013–2015 eruptions during the rising phase could have allowed for this feature to be missed. We suggest this feature is a general trend and not connected to the shorter SSS phase of 2016. However, to confirm it, we encourage very early detection and dense observations during the rise phase in all UVOIR bands of future eruptions.

The time of maxima was calculated from the quadratic model fits to the data near the peak. The peak magnitudes and the time of the peak are given in Table 4.

### 3.3.2. The Initial Steep Decline

The initial decline is very fast in all the bands. The decline rates during this phase are modeled by a straight line fit from  $t_{\max}$  to  $t = 3.5$  days after the eruption. The  $uvw2$  decline rate of  $0.93 \text{ mag day}^{-1}$  is steeper than the  $uvw1$  decline rate ( $0.78 \text{ mag day}^{-1}$ ) reported by Henze et al. (2018e). In the 2017–2022 data, we find that the  $g'$ -band decline rate ( $0.90 \text{ mag day}^{-1}$ ) is marginally higher than that for the  $r'$  band ( $0.88 \text{ mag day}^{-1}$ ), but when we combine it with the 2013–2015 data, the  $g'$ -band decline rate ( $0.90 \text{ mag day}^{-1}$ ) is less than that for the  $r'$  band ( $0.97 \text{ mag day}^{-1}$ ). Darnley et al. (2016) noted that the decline is fastest in  $V$  ( $1.21 \text{ mag day}^{-1}$ ) whereas the  $B$

and  $r'$  decline rates (in magnitude per day) are 0.99 and 0.97 respectively. The decline rates in this phase are used to derive the  $t_2$  times given in Table 4.

### 3.3.3. The Slow Decline

The slow decline phase is modeled with a linear fit from day 3.5 onward. This phase consists of the plateau in the light curves, which is also coincident with the SSS phase in X-rays. Combining all eruptions from 2013 gives a sufficient number of data points in all the filters for modeling except in  $g'$ . The decline rate during this phase is low in all the bands (see Table 4). The  $r'$  band also shows scatter during this linear decline, but these jitters are more prominent in the  $uvw2$  filter. The  $t_3$  times calculated from the straight line fits are 6.17, 10.83, and 14.15 days in  $r'i'$  and  $uvw2$ , respectively. The slowing down of the decline rate can be attributed to the expanding ejecta cooling at  $t \geq 4$  days from the eruption. It is also reflected in the color evolution where, after day 4, we see the system become redder (see Figure 3; and Figure 2 of Darnley et al. 2016). Beyond day 8, in  $uvw2$ , we see a further decrease in the decline rate and model it with a different slope. Optical photometry is sparse after day 8, but some data points in the  $i'$  band are available, although not enough for modeling. The  $i'$ -band excess (0.2–0.4 mag) around day 8 is most notable. This bump is traced by GP regression and is shown in blue in Figure 4.



**Table 4**  
Multi-eruption Light-curve Model Parameters

Filter	$t_{\max}^a$ (days)	$m_{\max}$ (AB)	$t_2$ (days)	$t_3$ (days)	Decline Rates (mag day <sup>-1</sup> )		
					$t_{\max}$ to 3.5	3.5 to $\sim 8$	$>8$
2017–2022							
<i>uvw2</i>	0.66 ± 0.26	18.82 ± 0.30	4.41 ± 0.51	14.15 ± 0.41	0.93 ± 0.03	0.17 ± 0.02	0.09 ± 0.01
<i>g'</i>	0.86 ± 0.04	18.27 ± 0.16	2.13 ± 0.04	...	0.90 ± 0.02	...	...
<i>r'</i>	0.86 ± 0.09	18.21 ± 0.27	2.37 ± 0.05	5.87 ± 5.61	0.88 ± 0.02	0.19 ± 0.18	...
<i>i'</i>	0.88 ± 0.12	18.30 ± 0.62	3.26 ± 0.20	...	0.56 ± 0.04	...	...
2013–2022 (Excluding 2016)							
<i>uvw2</i>	0.66 ± 0.26	18.82 ± 0.30	4.41 ± 0.51	14.15 ± 0.41	0.93 ± 0.03	0.17 ± 0.02	0.09 ± 0.01
<i>g'</i>	0.86 ± 0.04	18.27 ± 0.16	2.13 ± 0.04	...	0.90 ± 0.02	...	...
<i>r'</i>	0.97 ± 0.02	18.44 ± 0.03	2.29 ± 0.01	6.44 ± 0.08	0.97 ± 0.01	0.21 ± 0.02	...
<i>i'</i>	1.14 ± 0.06	18.63 ± 0.10	2.42 ± 0.02	10.83 ± 0.32	0.88 ± 0.01	0.10 ± 0.01	...

**Note.**

<sup>a</sup> Days since eruption.

During this phase, we see a secular trend of decreasing flux with undulations on top of it. This scatter from the smooth decline in *uvw2* has been discussed in Section 6. Toward the end of the final decline phase, when the SSS flux drops to zero at  $t > 18$ , we see a brief period of UV rebrightening before fading away to quiescent.

## 4. Optical Spectroscopy

### 4.1. Spectral Analysis

The optical spectra with good S/N are shown in Figure 5 with important emission features marked. Spectra taken on 2021 November 14.8 UT and 2022 December 3.73 UT were noisy and have not been used for analysis. All the spectra have been dereddened using  $E(B - V) = 0.10$  (Darnley et al. 2017b). The spectra were taken within the first 3 days of the eruption and depict a blue continuum with hydrogen Balmer and He I (4471, 5876, 6678 Å) emission lines. Some epochs also show the He II (4686 Å) and the N III lines ( $\sim 4640$  Å). Based on a multieruption combined spectrum, Darnley et al. (2016) identify several other features in the spectrum. While these features are not seen in the individual spectra presented here, a few faint features could be identified in the merged spectra taken at similar epochs after outbursts. He I 4922 Å and N II 5679 Å were detected in the combined spectra of 2018 (1.14 days) and 2020 (1.11 days), and He II 4686 Å, He I 5016 Å, N II 5679 and 6346 Å, and Raman O VI 6830 Å could be identified in the late phase merged spectra of 2018 (1.94 days), 2022 (2.03 days), and 2016 (2.23 days).

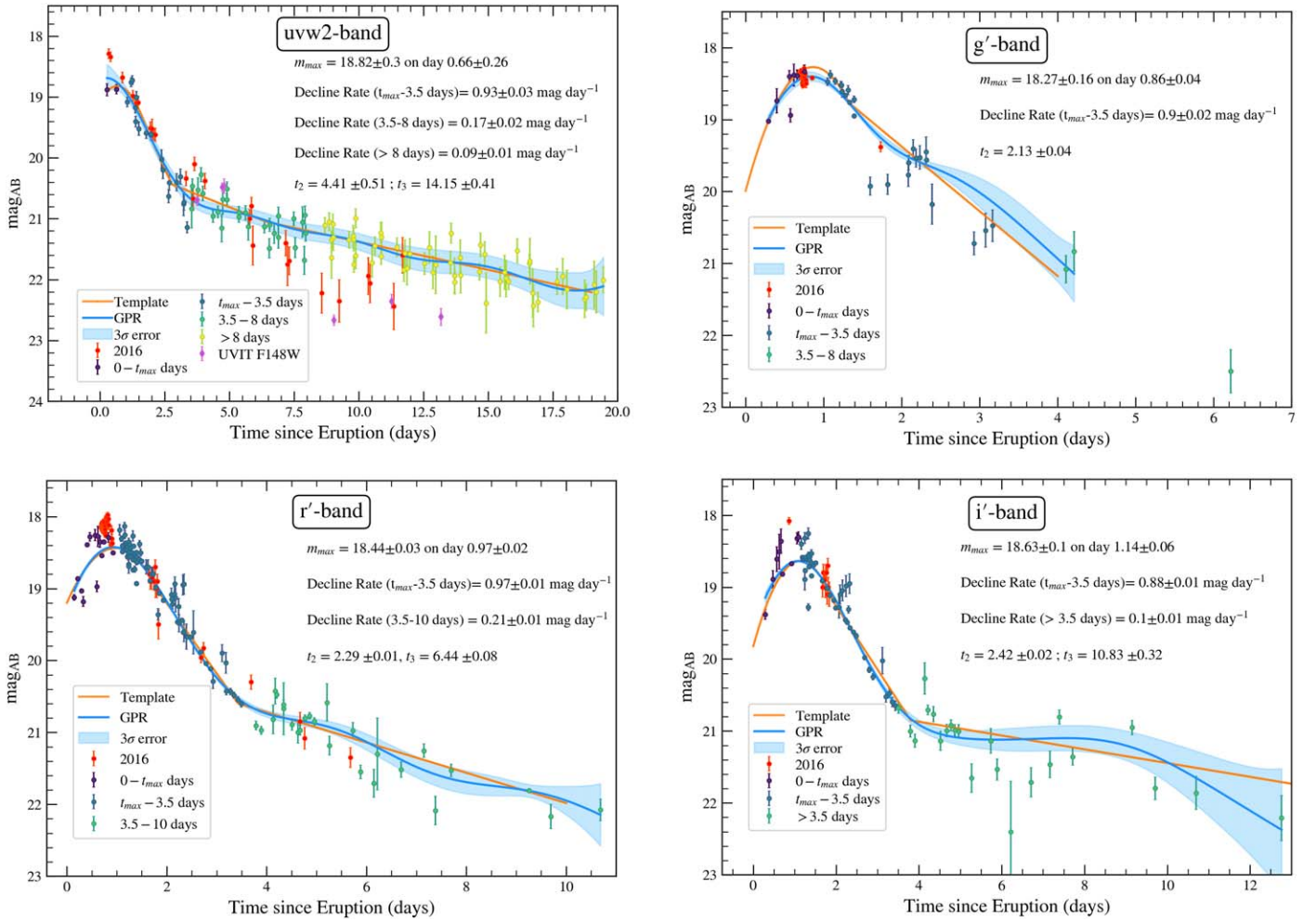
The line fluxes of the emission features clearly identifiable in the individual spectra are listed in Table 5. Also provided in the table are the FWHM velocities obtained from a Gaussian profile fit to the emission lines (using IRAF). The velocities calculated from the widths of the emission lines have been corrected for the instrumental response by deconvolving with the width of night skylines. The initial velocities within 1 day of eruption are as high as 5000 km s<sup>-1</sup>, typical of very fast novae. These observations are consistent with the previous eruptions of M31N 2008-12a (Darnley et al. 2015c, 2016; Henze et al. 2018e). At around  $\gtrsim 1.5$  days after the eruption, the emission-line widths narrow to 3000 km s<sup>-1</sup>. The narrowing of

the emission lines could be caused by the expansion and dissipation of the faster-moving component (Shore et al. 1996) or by the interaction of the ejecta with the circumbinary material. We find the line velocity decelerating at  $v_{\text{exp}} \propto t^{-0.27 \pm 0.07}$ . This is similar to the estimate provided by Darnley et al. (2016) ( $v_{\text{exp}} \propto t^{-0.28 \pm 0.05}$ ), who argue that the deceleration is due to the interaction of the ejecta with the circumbinary medium, and that the ejecta is in Phase II of the shocked remnant development (Bode & Kahn 1985).

The H $\alpha$  profile, as seen in Figure 5, indicates that the ejecta geometry is structured and time dependent. The temporal evolution of the H $\alpha$  line shows a double-peaked structure, prominent in the 2016, 2019, 2020, and 2021 spectra, taken around 0.9–1.5 days after the respective eruptions. Around 2 days after the eruption, the double-peaked profiles give way to a relatively narrow boxy profile.

### 4.2. Estimation of Physical Parameters

To understand the physical conditions in the nova ejecta, the spectral synthesis code Cloudy (v17.02; Ferland et al. 2017) was used to obtain a 1D model using the procedure described in Pavana (2020). We generated a 1D model for the best S/N spectra taken on 2018 November 8.6 UT and 2019 November 7.6 UT. The top left (bottom left) panel of Figure 6 shows the 2018 (2019) synthetic spectrum obtained using a two-component (diffuse+clumps) model. In the 2018 spectrum, the effective temperature and luminosity of the central ionizing source were found to be  $1.06 \times 10^5$  K and  $10^{37}$  erg s<sup>-1</sup> respectively. A clump component and a low-density diffuse component of density  $10^{11}$  and  $10^{10}$  cm<sup>-3</sup> respectively were used to fit the emission lines in the observed spectrum. The ejected mass and helium abundance from the best-fit modeled spectrum were found to be  $7.21 \times 10^{-8} M_{\odot}$  and  $2.47 \pm 0.11 \text{ He}_{\odot}$  respectively using the relations given in Pavana et al. (2019) and references therein. For the 2019 spectrum, the effective temperature and luminosity of the central ionizing source were  $7.20 \times 10^4$  K and  $10^{37}$  erg s<sup>-1</sup> respectively. A clump component of  $2.24 \times 10^{10}$  cm<sup>-3</sup> and a diffuse component of  $1.26 \times 10^8$  cm<sup>-3</sup> could generate a synthetic spectrum close to the observed one. The ejected mass and helium abundance, in this case, were found to be



**Figure 4.** Light-curve properties of 2013–2022 (except 2016) eruptions for  $uvw2$ ,  $g'$ ,  $i'$ , and  $r'$  bands (clockwise from top left). Outlier data points of 2016 are marked in red. The light-curve template, in orange, was generated by stitching the phases in each filter. GP mean and  $3\sigma$  error functions are shown in blue.

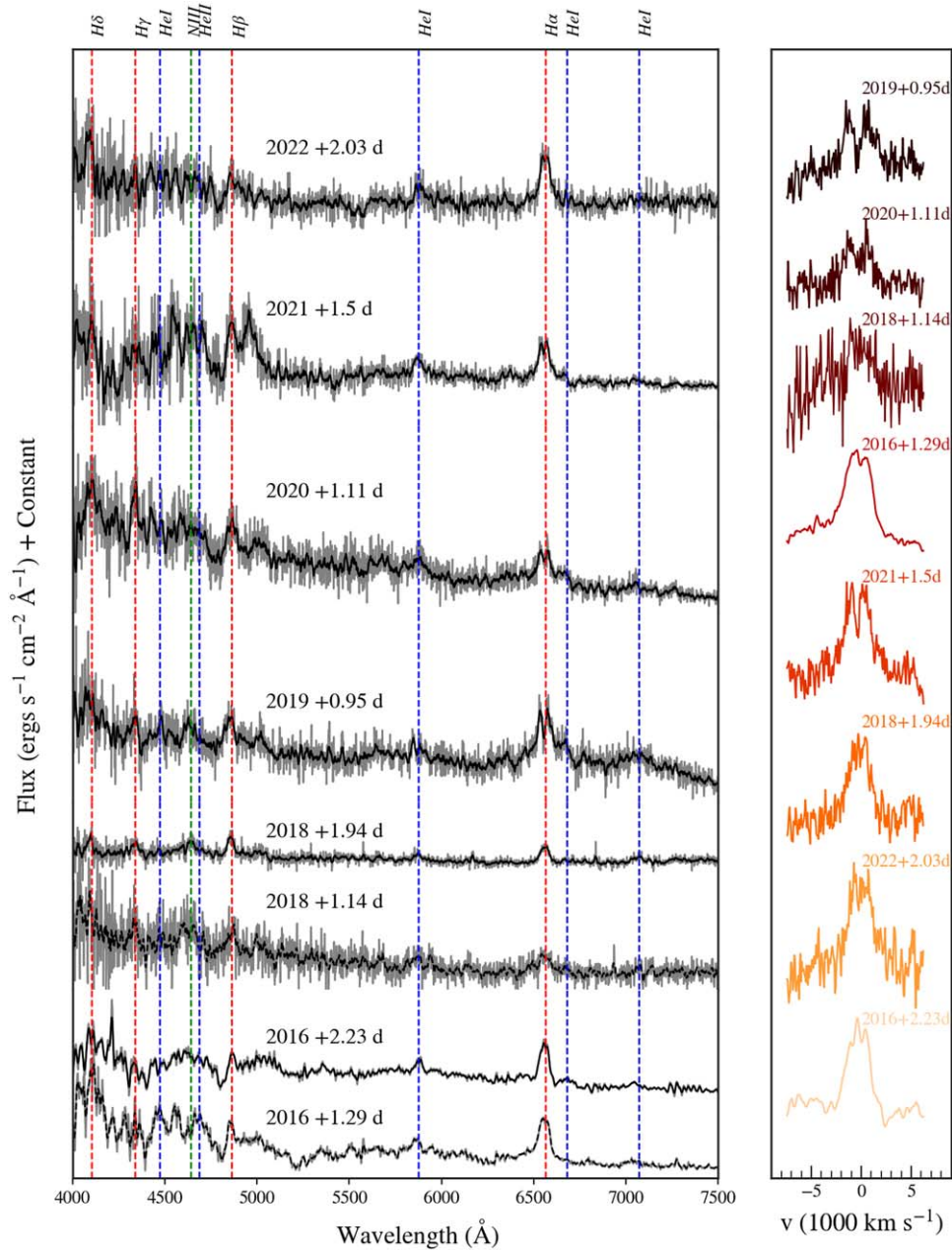
$1.3 \times 10^{-8} M_{\odot}$  and  $3.09 \pm 0.18 \text{ He}_{\odot}$  respectively. The ejected mass derived from X-rays (see Section 5.1) and spectral modeling are similar to that reported for the 2015 eruption by Darnley et al. (2016). An overabundance of helium has been estimated in other RNe such as RS Oph, V3890 Sgr, T Pyx (see Anupama & Pavana 2020 and references therein), and V745 Sco (Mondal et al. 2020).

It was noted that the two-component model was insufficient to generate the synthetic spectrum with a high  $\chi^2$  value. The observed spectrum shows N II lines, which were clearly visible once a third, diffuse, component was introduced to the model. This implies that the N II and He lines are clearly originating from different regions with different physical conditions. However, since the optical spectrum of this extragalactic nova has low S/N, modeling with three components is beyond the scope of this work. With these uncertainties, modeling a high S/N spectrum with similar methods in the upcoming eruptions is recommended.

The  $H\alpha$  emission-line profile during the 2018 and 2019 eruptions with multiple peaks encouraged us to obtain the morpho-kinematic structure for the ejecta using Shape (Steffen et al. 2011). We carried out the morpho-kinematic analysis of the  $H\alpha$  (and  $H\beta$  for 2018) velocity profile following the procedure described in Pavana (2020).

An asymmetric bipolar structure with bipolar cones and an equatorial ring (Figure 6) with a best-fit inclination angle of  $80^{\circ}75 \pm 1^{\circ}21$  could generate the synthetic velocity profile of 2018 spectrum. The extended bipolar component stretched up to  $4.52 \times 10^{12}$  cm along the ejecta axis from the center while the central bipolar cones (opening angle of  $\sim 91^{\circ}$ ) extended up to  $3.62 \times 10^{11}$  cm. The inner radius of the equatorial ring and radii of the bipolar cones were  $1.27 \times 10^{11}$  cm and  $5.42 \times 10^{11}$  cm, respectively. A similar geometry with a best-fit inclination angle of  $79^{\circ}60 \pm 1^{\circ}45$  could generate the synthetic  $H\alpha$  velocity profile of the 2019 spectrum shown in the bottom panel of Figure 6. The size of the extended bipolar component and the bipolar cone in the central region (opening angle of  $\sim 40^{\circ}$ ) were  $5.58 \times 10^{13}$  cm and  $6.16 \times 10^{12}$  cm along the ejecta axis from the center respectively. The inner radius of the equatorial ring and the radius of the bipolar cones were  $4.12 \times 10^{12}$  cm and  $5.27 \times 10^{12}$  cm, respectively. It should be noted that the He I (6678 Å) profile is blended with the broad  $H\alpha$  profile, and interestingly, the He I line arises from the inner bipolar cone region.

The outer part of the equatorial ring, the central bipolar cone, and the extended bipolar region are discernible in the models shown in Figure 6. The extended bipolar nature suggests a fast-moving polar ejecta along the ejecta axis, i.e., jets, contributing more to the high-velocity hydrogen Balmer emission.



**Figure 5.** Left: optical spectra obtained from HCT during 2016, and 2018–2022 eruptions of M31N 2008-12a. Right: time evolution of H $\alpha$  morphology from top to bottom.

## 5. The Supersoft Phase in X-Ray

### 5.1. X-Ray Light Curve

Figure 7 shows the light curve of supersoft X-ray emission during the 2017–2022 eruptions. The light curves from the previous eruptions are also shown for comparison. The emergence of the SSS phase is marked by the detections at  $\sim 8 \times 10^{-3} \text{ counts s}^{-1}$ , which increases to  $(3\text{--}4) \times 10^{-2} \text{ counts s}^{-1}$  and stays around that level from 8 to 15 days after the eruption. This *peak* of the SSS phase coincides with the UV light-curve plateau region. The mean turn-on and turn-off time of the nova estimated from the mid-points of detections and nondetections of 2014–2022 eruptions are  $5.06 \pm 0.60$  and  $16.89 \pm 0.96$  days, respectively from the time of the eruption. The average SSS duration of the nova is  $11.83 \pm 1.56$  days. Through the rise and during the SSS phase,

the X-ray emission is variable, while the decline from the SSS phase is relatively smooth. Multiple “dips” are seen in the 2017–2022 XRT light curves, one around days 6–8, and an even more noticeable one around days 10–11. This drop in the count rate is evident in the SXT light curves of 2020–2021 eruptions (Figure 7). Variability in the X-ray emission during the SSS phase has also been noted in the previous eruptions by Darnley et al. (2016), Henze et al. (2018e). The cause of this variability is not yet clear, and further high-cadence observations are required to understand its origin. We also note the unique short and faint nature of the SSS phase in the 2016 eruption compared to other eruptions, which is quite apparent in Figure 7.

To model the rise and decline in soft X-ray flux, we used a simple quadratic function. We included all the observations from 2013, except the peculiar 2016 eruption as its effect was



**Table 5**  
Flux and FWHM Velocities of Identified Lines in the Spectra

Identification		2016 (+2.23 days)			2018 (+1.94 days)			2019 (+0.95 day)		
		$\lambda$ (Å)	Flux $\times 10^{-15}$ (erg cm $^{-2}$ s $^{-1}$ )	Velocity (km s $^{-1}$ )	$\lambda$ (Å)	Flux $\times 10^{-15}$ (erg cm $^{-2}$ s $^{-1}$ )	Velocity (km s $^{-1}$ )	$\lambda$ (Å)	Flux $\times 10^{-15}$ (erg cm $^{-2}$ s $^{-1}$ )	Velocity (km s $^{-1}$ )
4101	H I	...	...	...	4094.52	2.37 $\pm$ 0.60	1954 $\pm$ 226	...	...	...
4340	H I	4333.90	2.54 $\pm$ 0.70	1952 $\pm$ 271	4340.02	2.61 $\pm$ 0.41	3546 $\pm$ 416	4335.70	4.08 $\pm$ 0.39	2274 $\pm$ 272
4471	He I	4489.07	0.96 $\pm$ 0.30	1637 $\pm$ 258	4468.84	1.95 $\pm$ 0.47	2618 $\pm$ 409	...	...	...
4640	N III	...	...	...	4642.11	2.01 $\pm$ 0.42	2386 $\pm$ 279	4632.18	6.42 $\pm$ 0.51	4113 $\pm$ 233
4861	H I	4862.06	3.32 $\pm$ 0.91	2233 $\pm$ 472	4856.94	3.35 $\pm$ 0.44	2278 $\pm$ 162	4850.50	6.80 $\pm$ 0.50	3121 $\pm$ 158
5876	He I	5877.73	1.77 $\pm$ 0.37	1974 $\pm$ 217	5871.05	1.22 $\pm$ 0.45	2023 $\pm$ 336	5861.49	1.76 $\pm$ 0.25	3092 $\pm$ 292
6563	H I	6556.99	8.15 $\pm$ 0.39	2407 $\pm$ 73	6558.89	4.42 $\pm$ 0.83	2581 $\pm$ 206	6559.45	23.20 $\pm$ 1.99	5099 $\pm$ 180
6678	He I	6678.70	1.79 $\pm$ 0.50	3024 $\pm$ 477	6667.21	0.57 $\pm$ 0.12	1235 $\pm$ 195	6671.71	3.63 $\pm$ 0.61	1921 $\pm$ 172
7065	He I	7042.55	1.34 $\pm$ 0.08	2655 $\pm$ 191	7064.87	1.79 $\pm$ 0.21	3144 $\pm$ 210	...	...	...
Identification		2020 (+1.11 days)			2021 (+1.50 days)			2022 (+2.03 days)		
		$\lambda$ (Å)	Flux $\times 10^{-15}$ (erg cm $^{-2}$ s $^{-1}$ )	Velocity (km s $^{-1}$ )	$\lambda$ (Å)	Flux $\times 10^{-15}$ (erg cm $^{-2}$ s $^{-1}$ )	Velocity (km s $^{-1}$ )	$\lambda$ (Å)	Flux $\times 10^{-15}$ (erg cm $^{-2}$ s $^{-1}$ )	Velocity (km s $^{-1}$ )
...	...	...	...	...	...	...	...	...	...	...
...	...	...	...	...	...	...	...	...	...	...
4101	H I	...	...	...	...	...	...	...	...	...
4340	H I	4336.68	6.65 $\pm$ 0.27	2000 $\pm$ 52	...	...	...	...	...	...
4471	He I	...	...	...	...	...	...	...	...	...
4640	N III	...	...	...	...	...	...	...	...	...
4861	H I	4861.88	8.65 $\pm$ 0.55	3549 $\pm$ 143	4863.05	14.8 $\pm$ 2.57	3055 $\pm$ 398	4870.23	6.25 $\pm$ 1.38	4015 $\pm$ 472
5876	He I	5878.37	4.19 $\pm$ 1.13	3598 $\pm$ 576	5871.49	5.20 $\pm$ 0.60	2370 $\pm$ 139	5880.52	4.69 $\pm$ 0.32	2839 $\pm$ 122
6563	H I	6557.92	10.24 $\pm$ 1.47	4011 $\pm$ 336	6556.97	18.80 $\pm$ 0.16	3564 $\pm$ 56	6562.23	15.40 $\pm$ 0.37	2924 $\pm$ 53
6678	He I	6661.61	2.92 $\pm$ 0.10	2330 $\pm$ 52	6663.74	1.73 $\pm$ 0.12	1343 $\pm$ 52	...	...	...
7065	He I	7044.02	1.53 $\pm$ 0.35	2386 $\pm$ 447	7051.42	1.29 $\pm$ 0.10	1940 $\pm$ 112	...	...	...

seen most in the SSS phase. We plot all the individual and binned sets in Figure 8. Deviations from the naive quadratic function are evident, especially the peaks at days 9–10 and 11–12 and the dips at days 7–8 and 10–11. The prominent features between days 8 and 13 are present in the binned and unbinned data, indicating that these variabilities’ causes last for more than half a day. The drop and rise of flux between days 10–11 seem to be general features of the SSS phase of M31N 2008-12a. Most of the variability is seen up to day 13; whereafter, the decline is relatively smooth.

X-ray studies of M31 novae (Henze et al. 2010, 2011, 2014b) have revealed the correlation of ejecta expansion velocity and the SSS  $t_{\text{on}}$  time. The ejecta mass was calculated from the turn-on times and the ejecta velocities ( $v_{\text{exp}}$ ) using the relation given in Henze et al. (2014b). A  $t_{\text{on}}$  time of  $\sim 5$  days with an  $v_{\text{exp}}$  of  $\approx 2000 \pm 200$  km s $^{-1}$  around this phase gives an ejecta mass range of  $4.2 \times 10^{-8} < M_{\text{ej,H}}/M_{\odot} < 10.2 \times 10^{-8}$ . These are slightly higher than that calculated from optical spectra in Section 4.2 but less than the average mass accreted in a year.

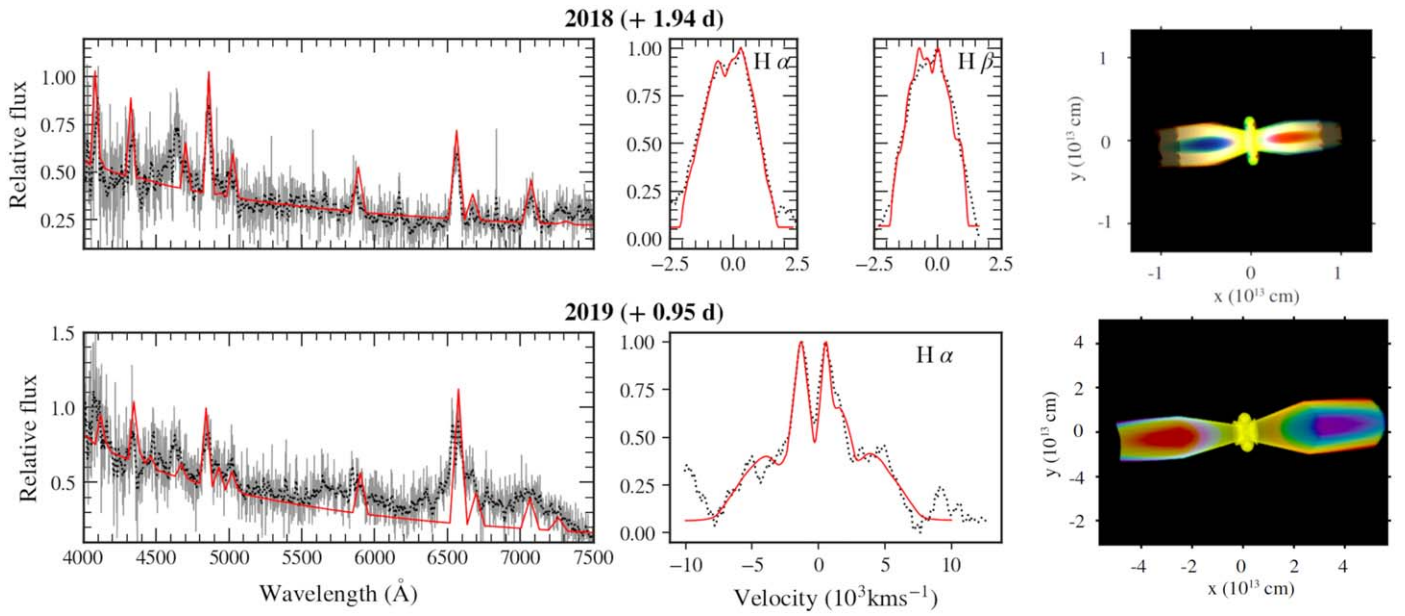
### 5.2. X-Ray Spectroscopy

The XRT data were also used to extract spectra by merging two data sets obtained on consecutive days to increase the S/N. We fixed the H column density at  $1.4 \times 10^{21}$  cm $^{-2}$  (Darnley et al. 2016) but varied the blackbody temperature and normalization to attain the best-fit values. The time evolution of the SSS temperature is shown in Figure 8 for 2017–2022 eruptions. Not only do the fluxes peak 10–14 days after the eruption, but the temperatures also peak, suggesting a correlation between the SSS flux and temperature. In the 2020 eruption, a temperature fluctuation during the maxima can

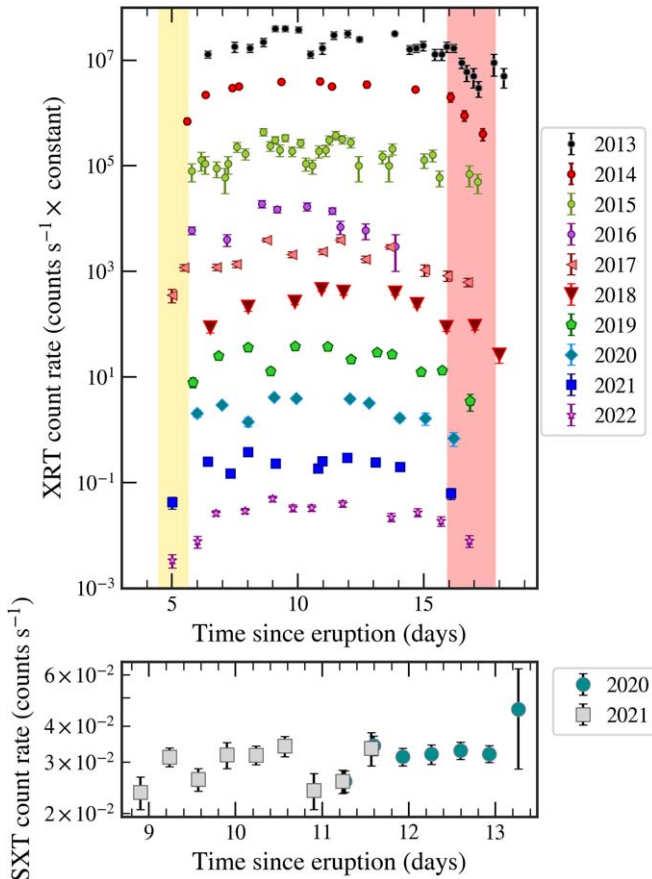
be seen. Such fluctuations have been reported before by Darnley et al. (2016). This pattern is not seen in other eruptions, possibly due to combining data sets of two consecutive days. In Section 5.1, it was noted that the rise to the maxima in the SSS phase shows variability, whereas the decline was smooth. The temperature evolution in Figure 8 also shows an asymmetry during the rise and decline of the SSS phase. These could be because of two different underlying causes. The increase in flux and temperature is due to the expansion and thinning of the ejecta, probing the deeper and hotter layers toward the WD surface. Whereas, during the later stage, when the obscuring material is already dissipated, the decrease in flux and temperature is because of the residual nuclear burning slowing down and eventually stopping.

Spectra extracted from the merged SXT data are shown in Figure 9. Also shown are the contemporaneous XRT spectra obtained from merged snapshots of 2 successive days. The data have been restricted to below 2.5 keV for the SXT to avoid background contamination due to its large PSF compared to the XRT. Beyond 1 keV, the flux is too low, owing to the supersoft nature of the source. A faint hard X-ray tail (above 1.5 keV) can be seen in SXT data, but we could not be certain of its origin because of low S/N. The best-fit blackbody temperatures from SXT spectra are slightly higher than the XRT data during similar times (Figure 8). The modeled flux in the 0.3–2.0 keV range was similar in the 2020 spectra for both instruments but differed by a factor of 2 (higher in SXT) in the 2021 spectra. As the observations are not continuous and the XRT and SXT epochs do not coincide exactly, the mismatch could be because of the rapid variability seen in flux and temperature during the SSS phase in recurrent novae.





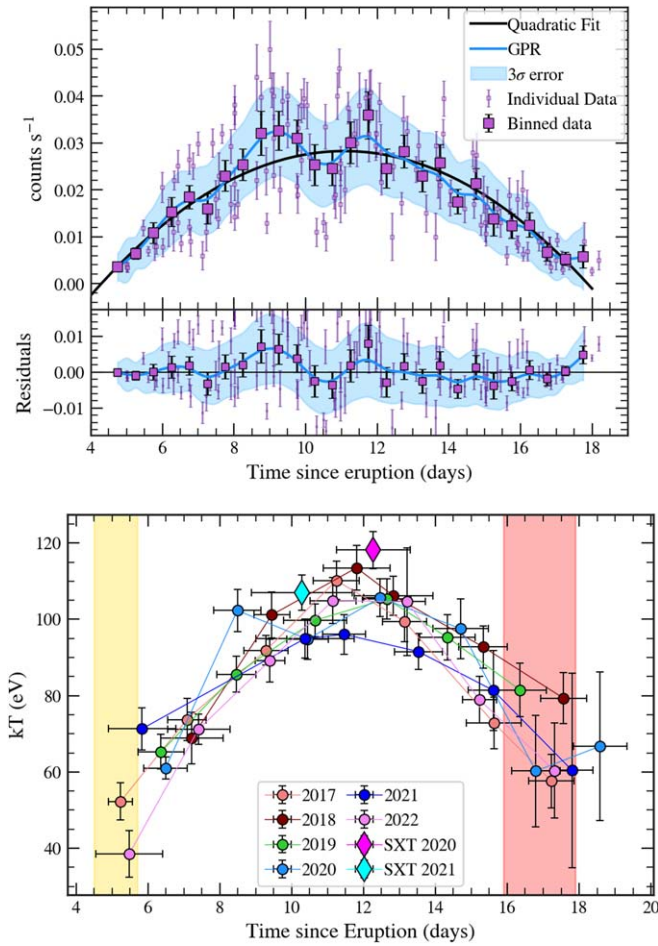
**Figure 6.** Top (from left): best-fit `CLOUDY` modeled spectrum (red) overlotted on the observed spectrum (gray) and smoothed spectrum (black dotted lines) of the 2018 eruption. Best-fit  $H\alpha$  and  $H\beta$  velocity profiles (red) overlotted on the observed profile (dotted line). Morphology of the ejecta of 2018 eruption obtained from `Shape` using  $H\alpha$  and  $H\beta$  velocity profiles. X-axis is the line-of-sight direction; Y-axis is perpendicular to the plane of sky and line of sight. Red represents velocity away from us, and violet toward us ( $2500$  to  $-2500$   $\text{km s}^{-1}$ ). Bottom (from left): same as top panel, but for 2019 eruption. Velocities are color coded from  $6000$   $\text{km s}^{-1}$  (red) to  $-6000$   $\text{km s}^{-1}$  (violet). Note that the scales are different in the ejecta morphology plot.



**Figure 7.** XRT (2013–2022) and SXT (2020–2021) light curves of M31N 2008-12a during its SSS phase. The SSS turn-on (yellow region) and turn-off (red region) times are also shown.

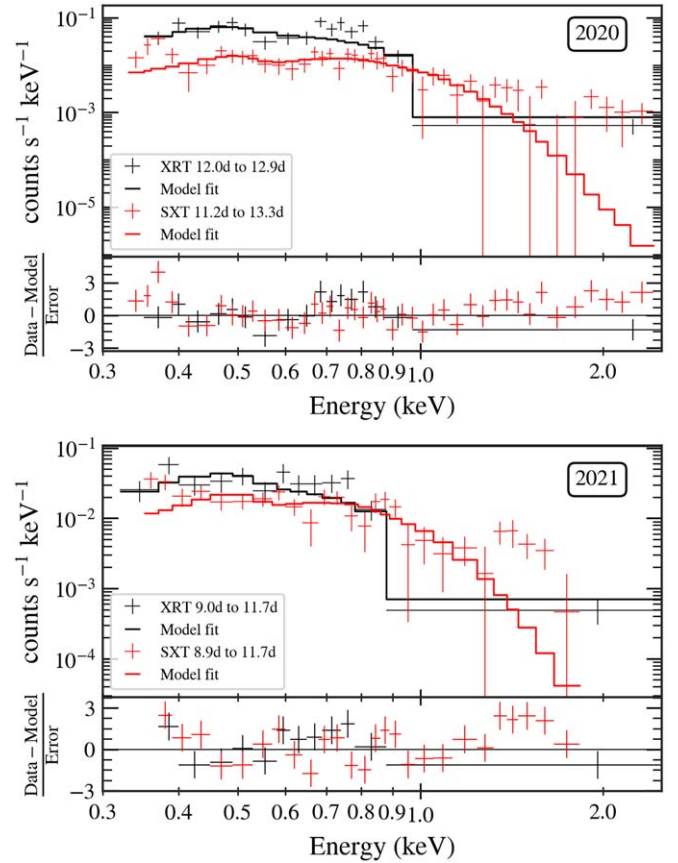
## 6. UV–X-Ray Correlation?

We noticed the 2016 *uvw2* light curve was *shorter and less luminous* compared to the 2017–2022 *uvw2* measurements during the SSS phase. Henze et al. (2018e) had found the same for soft X-rays and reasoned it to be due to a reduced accretion rate prior to the 2016 eruption. They could not comment on the 2016 *uvw2* measurements because of the unavailability of the *uvw2* light-curve template at that time. This motivated us to find the connection between these two wave bands in the supersoft phase. Since both soft X-ray and UV show different trends during the supersoft phase, it was necessary to detrend them. The *uvw2* light curves were detrended with a linear fit as it followed a linear declining trend during SSS phase, whereas the X-rays were detrended with a quadratic function as it followed a rise and a subsequent fall. The detrended light curves of each year from 2017 to 2022 are given in Figure 10. In 2017, we saw the UV and the X-ray fluxes behave inversely between days 7.5 and 13, and a Pearson correlation coefficient (hereafter  $r$ ) value of  $-0.76$  suggests a strong anticorrelation. In 2018, the anticorrelation lasts shorter from day 8.5 to 11.5 but is stronger with a  $r$  value of  $-0.86$ . 2019, on the other hand, does not show any strong correlation. In 2020 and 2022, there was a strong anticorrelation from day 9.5 to 14.5 when  $r$  value was  $-0.79$  and  $-0.68$ , respectively. The 2021 detrended light curves show mild anticorrelation ( $r = -0.38$ ), which is stronger than 2019 but weaker than the other eruptions during the days 9–14. This anticorrelation seen in most of the eruptions between UV and soft X-ray is strongest from day 8 to day 14 after the eruption, a time corresponding to the maxima of the SSS phase. UV and X-ray flux of most novae have been found to be uncorrelated (Page et al. 2022).



**Figure 8.** Top panel: combined XRT data of the SSS phase during 2013–2022 (except 2016) eruptions. Overplotted are data points binned at 0.5 day, its quadratic fit in black, GP regression and its corresponding  $3\sigma$  error region in blue. The deviations from the simple quadratic fit are shown below it. Bottom panel: temperature evolution from XRT data during the SSS phase of 2017–2022 eruptions. SXT data points for 2020 and 2021 are overplotted. Mean turn-on and turn-off times are marked in yellow and red, respectively.

Nonetheless, Ness et al. (2009) noted such anticorrelation of UV and X-rays in the detrended light curves for nova V458 Vul, although in the 0.6–10 keV X-ray range, just before the start of the SSS phase, and they suggested that it would imply that both the UV and hard X-rays originate from the same region. In HV Cet, the UV and X-ray flux were found to be tied up in phase, which Beardmore et al. (2012) argued to be due to the same cause, the orbital period in their case. V603 Aql also showed correlated UV–X-ray emission, although, in this case, it was interpreted as due to X-ray illumination (Borczyk et al. 2003). Since the source of soft X-rays during the SSS phase is the nuclear burning on the surface of the WD, the anticorrelation during the SSS peak, in our case, would hint that the UV radiation origin is also close to the surface of the WD. It is possible that the accretion disk survives each eruption (Darnley et al. 2017b, 2017c). The surviving partial accretion disk would emit UV radiation. The complete reformation of this partial disk could cause the variability seen in both UV and X-ray detrended light curves. The possibility of a wobbly, nascent accretion disk could also cause such a behavior.



**Figure 9.** XRT and SXT spectra of 2020 (top panel) and 2021 (bottom panel) eruptions. XRT data nearest to the SXT observation dates have been used for better comparison. The exact observation epochs are given in the legends (in days since the eruption). Spectral fitting involved a single blackbody with ISM absorption models for both SXT and XRT.

## 7. Recurrence Period, Accretion Rate, and WD Mass

M31N 2008-12a has erupted every year since 2008, making it an exceptional case of the only RN observed 15 times consecutively. This section focuses on the trend of the recurrence period and its relation to the accretion rate and the WD mass.

### 7.1. Increasing Recurrence Period

The mean recurrence period was reported to be  $P_{\text{rec}} = 351 \pm 13$  days after the 2015 eruption by Darnley et al. (2016), which was updated to  $363 \pm 52$  days after the outlier 2016 event by Henze et al. (2018e). Since the 2016 eruption, M31N 2008-12a erupted six more times, and each year, the time gap between two successive eruptions has been more than the mean recurrence period except in 2018 (310.1 days) and 2020 (355.9 days). As of the 2022 eruption, the mean recurrence period is  $P_{\text{rec}} = 363.6$  days with a standard deviation of 40.3 days (Figure 11, right panel). On the other hand, the median recurrence period has increased from 347 days in 2016 (Henze et al. 2018e) to 360.5 days in 2022. Figure 11 shows two different sets of histograms, along with their kernel density estimates (KDE), for the recurrence periods between 2008–2015 and 2008–2022. On considering up to the 2015 eruption (gray histogram in Figure 11), the mode of the recurrence period is 340 days, and the KDE peaks at

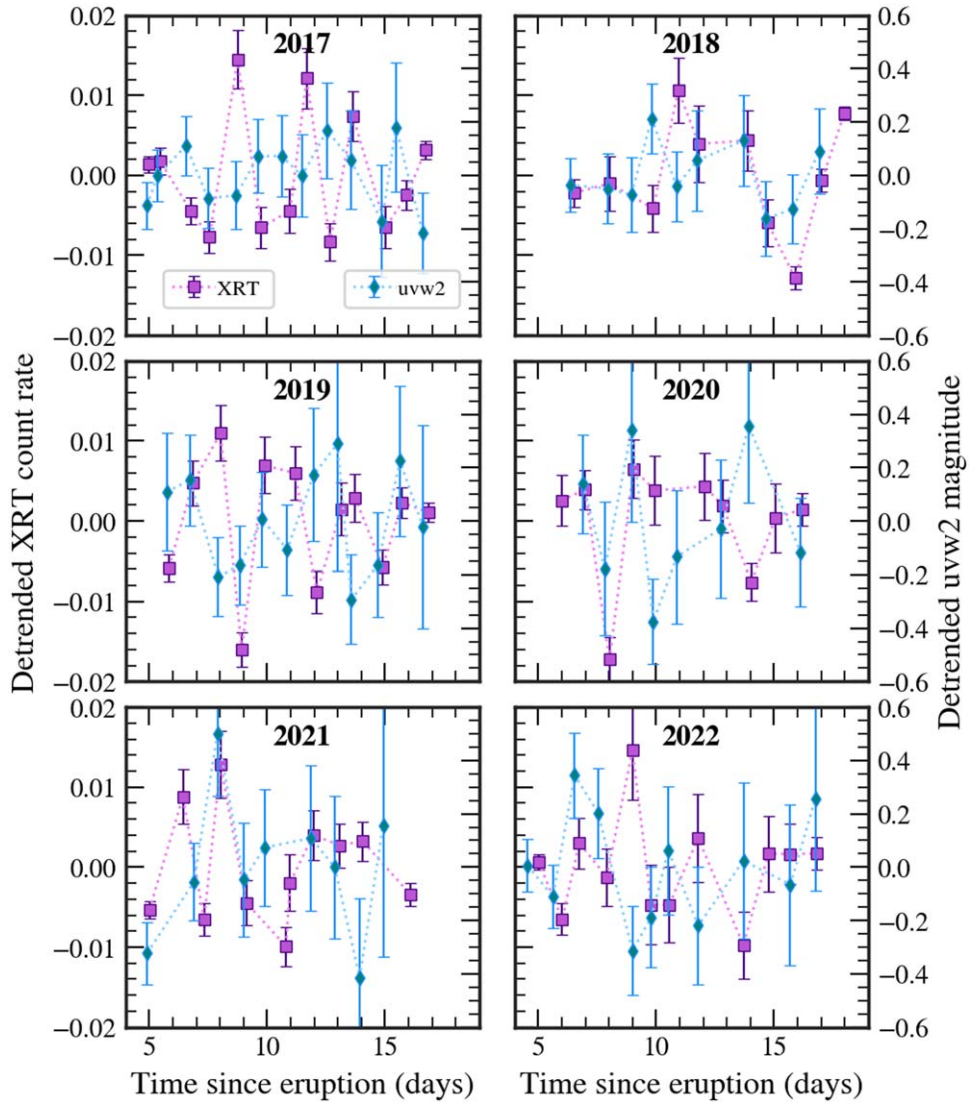


Figure 10. Detrended Swift *uvw2* and XRT light curves for 2017–2022 eruptions during the SSS phase.

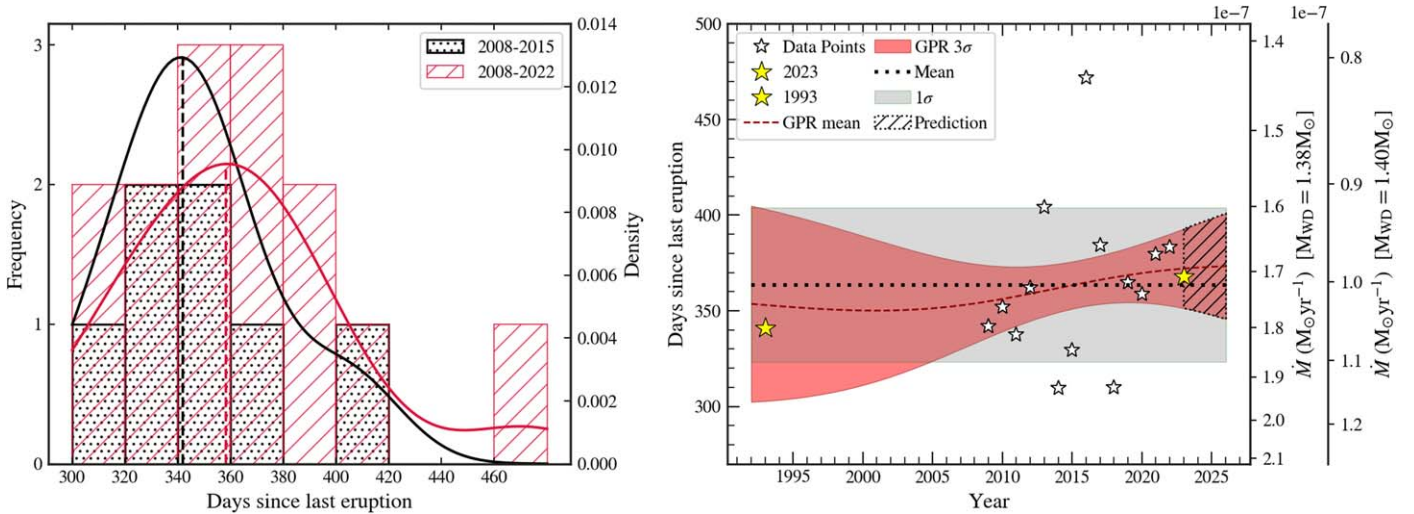


Figure 11. Left: distribution of the frequency of eruptions as a function of “days since the last eruption” binned at 20 days. Black histogram is for 2008–2015 eruption data, and black solid line represents the KDE for this data. Red histogram and red solid line represent the same for 2008–2022 data. Right: eruptions marked with stars. Dashed lines and colored areas represent the mean and error functions of the two models tracking the recurrence period with time. Shaded region is the projection for the 2023–2025 eruptions, given we do not see outlier events. Secondary  $Y$ -axes represent the accretion rates for  $1.38 M_{\odot}$  and  $1.40 M_{\odot}$  WD corresponding to the recurrence period on the primary  $y$ -axis.



341.28 days (FWHM of 67.27 days). But on incorporating all the eruption information until 2022 (red histogram in Figure 11), the mode of recurrence period shifts to 360 days with the KDE peaking at 358.18 days (FWHM of 96.36 days). Over the last 7 yr, we see a clear increasing trend in the recurrence period.

To further investigate this matter, we plotted the period as a function of the eruption year in the right panel of Figure 11. We used the GP regression technique to extract the trend in the data set and associate errors with it. The data were modeled using a Matern kernel with a typical length scale of 15 yr and an amplitude equal to the median of the recurrence period. We tested our model by applying it to the eruption dates of 2008–2021, and it could predict the 2022 eruption date within  $3\sigma$  error limits. The 2022 data were subsequently included in the training set to project the upcoming eruptions. Since there is a gap of around 15 yr between 1993 and 2008, we did not include the 1993 data point for our modeling, but an extrapolation of our model does seem to incorporate the 1993 eruption within error limits. For comparison, the mean and  $1\sigma$  of the constant recurrence period model have also been shown in Figure 11. Both of the models could reasonably anticipate the 2023 eruption. However, the GPR model can pick up any underlying data trends and better constrain the change in accretion rate.

We emphasize here that our model is restricted to only the *usual* eruptions that follow the trend. An anticipation of *outlier* events, such as the 2016 eruption, is not feasible.

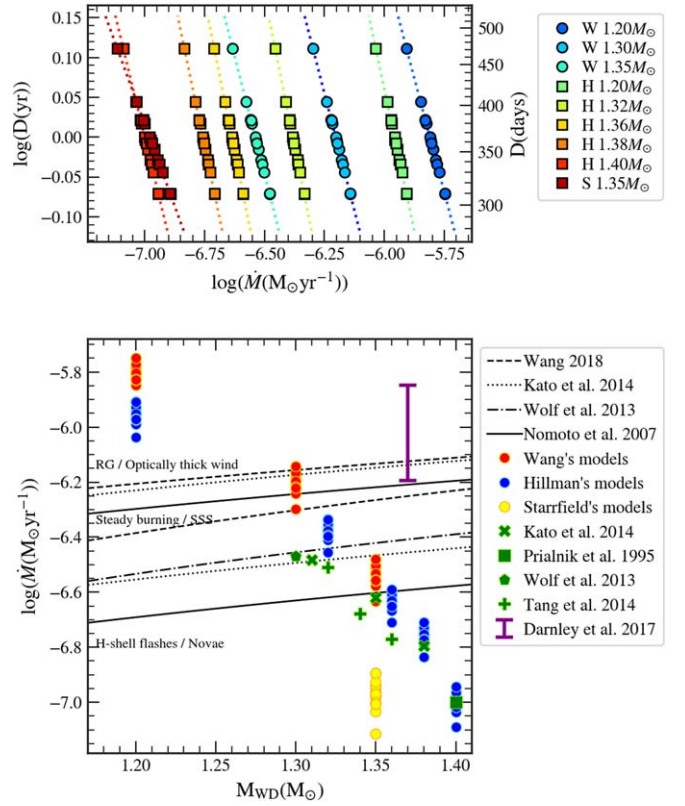
## 7.2. Estimating the WD Mass

In a theoretical study to understand the possible mass growth of a WD accreting matter from a nondegenerate companion, Hillman et al. (2016) have explored a range of accretion rates and derived limits on the accretion rate and on the initial mass that will allow a WD to reach the Chandrasekhar limit. Adopting their relation between  $D$  (period) and  $\dot{M}$  (accretion rate) for hydrogen accretion cases,  $\log \dot{M} = -A \log D - B$ , we estimate the accretion rates in the last 15 yr for the M31 RN eruptions. Here, the coefficients  $A$  and  $B$  depend on the WD mass. For each value of  $M_{\text{WD}}$ ,  $A$  and  $B$  were determined by fitting a linear function to the parameter space of  $\log D$  and  $\log \dot{M}$ . The accretion rates of WD masses between  $1.20 M_{\odot}$  and  $1.40 M_{\odot}$  corresponding to the periods of M31N 2008-12a are shown in the top panel of Figure 12.

Wang (2018) have used the Modules for Experiments in Stellar Astrophysics (MESA) to model the binary evolution of WD accreting H-rich material from a companion for a range of WD masses and accretion rates.

The composition of the accreted material was fixed at H:He:Metals  $\equiv$  70:28:2. We use their results for the massive WD cases ( $1.20$ – $1.35 M_{\odot}$ ), obtain a best-fit power-law relation between the accretion rate and the period, and employ the same to infer the accretion rates for each cycle of M31N 2008-12a. These are also shown in the top panel of Figure 12.

We plot the accretion rates thus obtained corresponding to the periods of M31N 2008-12a in the last 15 yr in the  $M_{\text{WD}}-\dot{M}$  parameter space in the bottom panel of Figure 12. For comparison, we overplot the results from Kato et al. (2014), Prialnik & Kovetz (1995), Wolf et al. (2013), and Tang et al. (2014), who predicted the WD mass and accretion rates for a recurrence period of 1 yr.



**Figure 12.** Top: observed recurrence period plotted against accretion rate for different WD masses. “W,” “H,” and “S” in the legend indicate accretion rates derived from Wang (2018), Hillman et al. (2016), and Starrfield (2017) respectively. Bottom:  $M_{\text{WD}}-\dot{M}$  parameter space for M31N 2008-12a. Accretion rates from the top panel are shown in red (Wang’s), blue (Hillman’s), and yellow (Starrfield’s). Overplotted in green markers are for the 1 yr recurrence period taken from the literature. Stable and critical accretion rate limits from four studies are shown as horizontal tracks. The accretion rate range obtained by Darnley et al. (2017c) during quiescence is shown in purple.

In the  $M_{\text{WD}}-\dot{M}$  plane, when the accretion rate surpasses the critical threshold ( $\dot{M} > \dot{M}_{\text{cr}}$ ), the WD exhibits an RG-like behavior, undergoing surface mass burning at the critical rate, while any excess material is ejected in the form of optically thick winds (Kato & Hachisu 1994; Hachisu et al. 1996). Conversely, when the accretion rate falls below the critical threshold but remains above the stable H accretion rate, i.e.,  $\dot{M}_{\text{cr}} > \dot{M} > \dot{M}_{\text{st}}$ , the burning on the WD’s surface remains stable, capable of sustaining itself over an extended period as a supersoft X-ray emitter (Kato et al. 2014). Below the stability line, i.e.,  $\dot{M}_{\text{st}} > \dot{M}$ , the accretion rate is insufficient to sustain continuous hydrogen burning. Systems within this parameter range experience *H-shell flashes* or nova eruptions, a category that includes all RNe, including M31N 2008-12a.

The limits on  $\dot{M}_{\text{cr}}$  and  $\dot{M}_{\text{st}}$  taken from Wang (2018), Kato et al. (2014), Wolf et al. (2013), and Nomoto et al. (2007) are shown in the bottom panel of Figure 12. The differences in these limits are primarily because of the different techniques employed in modeling.

We infer from Figure 12 (bottom panel) that a WD with mass below  $1.30 M_{\odot}$  has a high accretion rate and does not allow the RN phenomenon to occur at the rate of once a year.

We also see that  $1.32$ – $1.36 M_{\odot}$  WDs do fall into the *H-shell flash* region of some of the models, and any WD with  $M_{\text{WD}} > 1.36 M_{\odot}$  satisfies the necessary criteria of nova



eruption ( $\dot{M} < \dot{M}_{\text{st}}$ ) for all the models. Thus, the WD mass in M31N 2008-12a is likely to be greater than  $1.36 M_{\odot}$ , which would, in turn, allow *H-flash* features at the observed recurrence period of M31N 2008-12a.

However, it should be emphasized that Starrfield (2017) generated models using MESA, which allow for the stability line (and the critical line) to exist for less massive WDs but not for higher mass WDs ( $\sim 1.35 M_{\odot}$  model shown in Figure 12). It was shown that such massive WDs would show H-flashes initially, followed by He-flashes, and ultimately grow to  $M_{\text{Ch}}$ .

Strikingly, none of the models could predict the accretion rate derived from accretion disk modeling discussed in Darnley et al. (2017c). The accretion rate was found to vary during eruption, SSS, and quiescence phases. In Figure 12, we show the range of accretion rate onto the WD during quiescence. It may hint that Starrfield’s models, which do not predict any upper limit on stable accretion, are better suited for such massive systems. But at the same time, the accretion rates generated by both types of models (with and without an upper limit) are insufficient to match the ones derived from observations of this exceptional RN.

## 8. Discussion

### 8.1. More Evidence of Jets?

The cusp around maxima in the light curves has been suggested to have different origins. It could be due to shock from a secondary ejection (Kato et al. 2009), polar outflow along the line of sight, or ejecta–donor interaction (Darnley et al. 2018b). Observational evidence of broad-winged emission features supports the presence of a fast-moving component in the ejecta. Modeling the  $H\alpha$  (and  $H\beta$  for 2018) line profiles using *Shape* could also generate these fast-moving polar ejecta close to the line of sight. Darnley et al. (2017b) proposed the presence of these jets using HST data, although they did not confirm it. The photometric and spectroscopic evidence combined with  $H\alpha$  profile modeling presented in this work further strengthens the claim of polar jets emanating close to the line of sight, indicating a low-inclination angle for this system.

Optical imaging and spectroscopic modeling of RS Oph revealed the ejecta to be bipolar, possibly associated with jets (Bode et al. 2007; Ribeiro et al. 2009). RS Oph jets were confirmed in radio wave bands (O’Brien et al. 2006; Rupen et al. 2008; Sokoloski et al. 2008; Munari et al. 2022). High-velocity components of emission lines are standard signatures of jets and were observed in V1494 Aql (Iijima & Esenoglu 2003), U Sco (Kato & Hachisu 2003), V6568 Sgr, and YZ Ret (McLoughlin et al. 2021a). McLoughlin et al. (2021b) pointed out that jets are usually associated with fast novae, which are essentially linked to massive WDs. M31N 2008-12a falls perfectly into these categories. One possible mechanism for jet formation could include bipolar winds during the nova outburst and subsequent mass ejection into an asymmetric medium. This case is particularly interesting for RNe where the asphericity left behind from previous eruptions triggers material to escape through certain channels. Magnetic field lines near the WD and the accretion disk could also lead to the collimation of wind perpendicular to the disk (Ogilvie & Livio 2001). The accretion disk of M31N 2008-12a is known to be luminous (Darnley et al. 2017c). Such bright

disks can also give rise to supersonic winds forming jets (Fukue 2002).

### 8.2. Light Curve

The optical light curves from 2017 to 2022 are similar. A sharp linear decline is seen from day 1 since the maximum, followed by an approximately flat but jittery plateau, and then, the final decline ensues. The evolution is similar to the past eruptions and is close to the light curves of P-class recurrent novae (Strope et al. 2010).

The UV peak is observed before the optical peak in all the eruptions. The UV light curve shows a decline from peak magnitude until the onset of the plateau phase, followed by multiple jitters. The UV plateau phase is consistent with the SSS phase’s turn-on time. A flat decline follows it and ultimately ends with a brief period of brightening. The 2016 *uvw2* light curve shows considerable deviation from the other eruptions.

The SSS phase turns out to be similar in all the eruptions except for the 2016 eruption, where it ended as early as  $\sim 16$  days from the eruption. The SSS temperature is strongly correlated to the soft X-ray flux. There is a significant drop in X-ray flux during the 2017–2022 eruptions around the same time that was noted in the previous eruptions on day 11 since the eruption. The cause of this drop in flux is yet to be explored.

During the slow decline phase, the 2016 *uvw2* light curve (Figure 4) deviated from the general trend. Here, we also point out that, for the first time in 2016, detailed *uvw2* observations were conducted, and the light curve was found to be similar to the 2015 *uvw1* trend. Based on this, Henze et al. (2018e) concluded that the optical and UV evolution in the 2016 eruption were similar to the previous ones, while the peculiarity of the 2016 eruption was reflected only in the X-rays. However, Figures 2 and 4 show that the evolution of *uvw2* flux in 2016 differs from all other (subsequent) eruptions. The 2016 *uvw2* light curve is fainter, similar to what was also noted for its soft X-ray counterpart (Section 5.1).

### 8.3. Decreasing Accretion Rate

In Section 7, we found that the recurrence period shows an increasing trend with time. A modest increase in the recurrence period would imply that either the accretion rate or the WD mass is decreasing over the years (Hillman et al. 2016; Wang 2018). Light-curve models provided by Kato et al. (2015) suggested the WD to be as massive as  $1.38 M_{\odot}$ , accreting at a rate of  $1.3 \times 10^{-7} M_{\odot} \text{ yr}^{-1}$ . Whereas Darnley et al. (2017c) modeled the quiescent phase accretion disk using HST data and showed that the rate of mass accretion could be even higher at  $(0.6\text{--}1.4) \times 10^{-6} M_{\odot} \text{ yr}^{-1}$  considering a 50% efficiency. On the other hand, the ejecta masses during each nova cycle (see Sections 5.1 and 4.2) are  $\sim 10^{-8} M_{\odot}$ . Thus, the net mass lost during each eruption is always less than the total mass gained between each eruption. As a result, the WD is growing in mass with time. The absence of Ne lines in the spectra indicates it to be a CO WD. Such WDs can reach  $>1.36 M_{\odot}$  only by accreting material. These inferences rule out the possibility of an increasing recurrence period due to decreasing WD mass. We suspect that the accretion rate has been slowly declining over the years (see Figure 11), lengthening the time taken to reach the critical conditions

required for thermonuclear runaway reactions to be initiated on the surface of the WD. The following could cause a gradual decrease in the accretion rate:

1. the presence of starspots and increased activity in the secondary (Henze et al. 2018e);
2. the companion slowly running out of gas by supplying material to power the “H flashes” for millions of years (Darmley et al. 2019c);
3. the orbital dynamics can also change accretion rates, especially in violent systems like M31N 2008-12a, where nova eruptions are frequent;
4. the extent of the destruction of the accretion disk during each nova eruption decides the time taken to reform the accretion disk and resumption of accretion; delayed accretion can also lead to a slowing down of the recurrence period;
5. a third body orbiting the M31N 2008-12a cataclysmic variable (CV) could perturb the binary motion, changing the accretion rate; triple systems are known to produce exotic binaries; one such example is T Pyx (Knigge et al. 2022).

## 9. Summary

This paper presents the evolution of 2017–2022 eruptions of M31N 2008-12a in different wavelengths. The main results are summarized as follows.

1. The linear decline post-maximum in the optical light curves is similar to that of the previous eruptions. The evolution of the UV light curve in the 2017–2022 eruptions is also similar to the previous eruptions. A rapid decline since the maximum is followed by a plateau phase coincident with the SSS turn-on time. It then follows a secular decline with undulations before dimming beyond the detection limit. A UV rebrightening is also seen toward the end of the SSS phase.
2. The SSS phase features are consistent with previously reported values. The mean SSS turn-on time and turn-off time are  $5.1 \pm 0.6$  days and  $16.9 \pm 1.0$  days since the eruption, respectively. The SSS phase shows X-ray variability, the most prominent being the dip  $\sim 11$  days after the eruption.
3. The UV and soft X-ray flux are found to be anticorrelated at the peak of the SSS phase, which has not been reported before. This implies that both originate at the surface of the WD and could arise during the reformation of the partially disrupted accretion disk.
4. Balmer, He, and N lines dominate the optical spectra.  $H\alpha$  velocities decelerate from  $\sim 5000 \text{ km s}^{-1}$  within 1 day of eruption to  $\sim 2000 \text{ km s}^{-1}$  at around 4 days after eruption, consistent with phase II of shock remnant development.
5. The ejecta mass derived from  $t_{\text{on}}$  and Cloudy modeling is of the order of  $10^{-8}$ – $10^{-7} M_{\odot}$ , which is consistent with previous estimates derived using different techniques. Compared to the accretion rates derived in this work and previous studies, the ejecta mass is lower than the average mass accreted in a year, implying the WD is potentially increasing its mass.
6. He abundance in the ejecta was found to be high at  $\text{He}/\text{He}_{\odot} \sim 2.5$ – $3.1$ , as is the case for most RNe.

7.  $H\alpha$  line morphology indicates an ejecta with an equatorial ring, a slow bipolar conical component, and an extended fast bipolar component along the line of sight resembling a jet-like structure. Evidence of a cuspy feature in the light curves near the peak is seen as a general trend after the 2016 eruption in the  $r'$  and  $i'$  bands. Together with emission-line modeling, we conjecture the cusp is caused by jets present in the ejecta. The presence of jets in this system was suspected, and we provide strong evidence for its presence here. Such jets could be common in novae systems, especially RNe.
8. We noticed that the recurrence period shows a weak tendency to increase with time, a sign of a decreasing accretion rate.
9. By comparing the recurrence period with binary evolution models, the mass of the WD is constrained to be  $>1.36 M_{\odot}$ . However, we emphasize that none of the models could replicate the observed accretion rate determined in previous studies. Irrespective of that, a CO WD near the  $M_{\text{Ch}}$  and growing in mass is a good candidate for the single degenerate channel of Type Ia supernova explosions.

## Acknowledgments




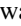
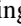
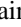




We would like to thank the anonymous referee for the valuable comments that improved the quality of this work. We are grateful to the support staff and the observers at VBO and IAO. We take this opportunity to thank the TAC for the time allocation for ToO observations. We thank the staff of IAO, Hanle, and CREST, Hosakote, that made these observations possible. The facilities at IAO, CREST, and VBO are operated by the Indian Institute of Astrophysics, Bangalore. We acknowledge the use of GROWTH-India telescope data. The GROWTH-India telescope (GIT) is a 70 cm telescope with a  $0^{\circ}.7$  field of view set up by the Indian Institute of Astrophysics (IIA) and the Indian Institute of Technology Bombay (IITB) with funding from the Indo-US Science and Technology Forum and the Science and Engineering Research Board, Department of Science and Technology, Government of India. It is located at the Indian Astronomical Observatory (IAO, Hanle). We acknowledge funding by the IITB alumni batch of 1994, which partially supports the operation of the telescope. Telescope technical details are available at <https://sites.google.com/view/growthindia/>. This work uses the SXT and UVIT data from the AstroSat mission of the Indian Space Research Organisation (ISRO). We thank the AstroSat TAC for allowing us ToO time to observe this nova from 2019 to 2022. We thank the SXT and UVIT payload operation centers for verifying and releasing the data via the ISSDC data archive and providing the necessary software tools. We acknowledge the use of public data from the Swift data archive. This work has also used software and/or web tools obtained from NASA’s High Energy Astrophysics Science Archive Research Center (HEASARC), a service of the Goddard Space Flight Center and the Smithsonian Astrophysical Observatory. K.P.S. and G.C.A. thank the Indian National Science Academy for support under the INSA Senior Scientist Programme.

*Facilities:* HCT; VBO:JCBT; GIT; Swift (UVOT and XRT); AstroSat (UVIT and SXT).

*Software:* CCDLAB (Postma & Leahy 2017), IRAF v2.16.1 (Tody 1993), HEASOFT v6.25, XIMAGE v4.5.1, and

XSELECT v2.4e (Nasa High Energy Astrophysics Science Archive Research Center (Heasarc) 2014), XSPEC v12.12.0 (Arnaud 1996), Python v3.6.6 (Van Rossum & Drake 2009), NumPy (Harris et al. 2020), SciPy (Virtanen et al. 2020), Pandas (McKinney 2010), Matplotlib (Hunter 2007), scikit-learn (Pedregosa et al. 2011), astroquery (Ginsburg et al. 2019).

### ORCID iDs

Judhajeet Basu  <https://orcid.org/0000-0001-7570-545X>  
 M. Pavana  <https://orcid.org/0000-0002-0000-1543>  
 G. C. Anupama  <https://orcid.org/0000-0003-3533-7183>  
 Sudhanshu Barway  <https://orcid.org/0000-0002-3927-5402>  
 Kulinder Pal Singh  <https://orcid.org/0000-0001-6952-3887>  
 Vishwajeet Swain  <https://orcid.org/0000-0002-7942-8477>  
 Shubham Srivastav  <https://orcid.org/0000-0003-4524-6883>  
 Harsh Kumar  <https://orcid.org/0000-0003-0871-4641>  
 Varun Bhalerao  <https://orcid.org/0000-0002-6112-7609>  
 L. S. Sonith  <https://orcid.org/0000-0002-2033-3051>

### References

- Agnihotri, V. K., & Raj, A. 2018a, *ATel*, **12189**, 1  
 Agnihotri, V. K., & Raj, A. 2018b, *ATel*, **12204**, 1  
 Agnihotri, V. K., Vora, K., Bisht, D., & Raj, A. 2022, *ATel*, **15787**, 1  
 Anupama, G. C., & Pavana, M. 2020, *JApA*, **41**, 43  
 Arnaud, K. A. 1996, in *ASP Conf. Ser.* 101, *Astronomical Data Analysis Software and Systems V*, ed. G. H. Jacoby & J. Barnes (San Francisco, CA: ASP), **17**  
 Balcon, C. 2023, *TNSCR*, **2023-3145**, 1  
 Barsukova, E., Fabrika, S., Hornoch, K., et al. 2011, *ATel*, **3725**, 1  
 Basu, J., Barway, S., Anupama, G. C., Chamoli, S., & Kumar, S. P. 2023, *ATel*, **16367**, 1  
 Basu, J., Barway, S., Anupama, G. C., & Sujith, D. S. 2022, *ATel*, **15790**, 1  
 Beardmore, A. P., Osborne, J. P., Page, K. L., et al. 2012, *A&A*, **545**, A116  
 Bertin, E., & Arnouts, S. 1996, *A&AS*, **117**, 393  
 Bertin, E., Mellier, Y., Radovich, M., et al. 2002, in *ASP Conf. Ser.* 281, *Astronomical Data Analysis Software and Systems XI*, ed. D. A. Bohlender, D. Durand, & T. H. Handley (San Francisco, CA: ASP), **228**  
 Bode, M. F., Harman, D. J., O'Brien, T. J., et al. 2007, *ApJL*, **665**, L63  
 Bode, M. F., & Kahn, F. D. 1985, *MNRAS*, **217**, 205  
 Borczyk, W., Schwarzenberg-Czerny, A., & Szkody, P. 2003, *A&A*, **405**, 663  
 Boyd, D., Hornoch, K., Henze, M., et al. 2017, *ATel*, **11116**, 1  
 Breeveld, A. A., Landsman, W., Holland, S. T., et al. 2011, in *AIP Conf. Proc.* 1358, *Gamma Ray Bursts 2010*, ed. J. E. McEnery, J. L. Racusin, & N. Gehrels (Melville, NY: AIP), **373**  
 Burrows, D. N., Hill, J. E., Nousek, J. A., et al. 2005, *SSRv*, **120**, 165  
 Darnley, M. J. 2020, *ATel*, **14138**, 1  
 Darnley, M. J., & Healy, M. W. 2022, *ATel*, **15788**, 1  
 Darnley, M. J., Healy, M. W., Henze, M., & Williams, S. C. 2017a, *ATel*, **11117**, 1  
 Darnley, M. J., Healy, M. W., Henze, M., & Williams, S. C. 2018a, *ATel*, **11149**, 1  
 Darnley, M. J., & Henze, M. 2020, *AdSpR*, **66**, 1147  
 Darnley, M. J., Henze, M., Bode, M. F., et al. 2016, *ApJ*, **833**, 149  
 Darnley, M. J., Henze, M., Hachisu, I., et al. 2019a, *ATel*, **13274**, 1  
 Darnley, M. J., Henze, M., Hachisu, I., et al. 2019b, *ATel*, **13290**, 1  
 Darnley, M. J., Henze, M., Shafter, A. W., & Kato, M. 2015a, *ATel*, **7964**, 1  
 Darnley, M. J., Henze, M., Shafter, A. W., & Kato, M. 2015b, *ATel*, **7965**, 1  
 Darnley, M. J., Henze, M., Shafter, A. W., et al. 2018b, *ATel*, **12177**, 1  
 Darnley, M. J., Henze, M., Shafter, A. W., et al. 2018c, *ATel*, **12179**, 1  
 Darnley, M. J., Henze, M., Steele, I. A., et al. 2015c, *A&A*, **580**, A45  
 Darnley, M. J., Hounsell, R., Godon, P., et al. 2017b, *ApJ*, **847**, 35  
 Darnley, M. J., Hounsell, R., Godon, P., et al. 2017c, *ApJ*, **849**, 96  
 Darnley, M. J., Hounsell, R., O'Brien, T. J., et al. 2019c, *Natur*, **565**, 460  
 Darnley, M. J., Oksanen, A., Henze, M., et al. 2019d, *ATel*, **13273**, 1  
 Darnley, M. J., & Pag, K. L. 2021a, *ATel*, **15040**, 1  
 Darnley, M. J., & Pag, K. L. 2021b, *ATel*, **15050**, 1  
 Darnley, M. J., & Page, K. L. 2020, *ATel*, **14142**, 1  
 Darnley, M. J., Page, K. L., & Healy, M. W. 2022, *ATel*, **15798**, 1  
 Darnley, M. J., Page, K. L., & Henz, M. 2020a, *ATel*, **14152**, 1  
 Darnley, M. J., Shafter, A. W., Kafka, S., Williams, S., & Henze, M. 2020b, *ATel*, **14130**, 1  
 Darnley, M. J., Williams, S. C., Bode, M. F., et al. 2014, *A&A*, **563**, L9  
 Engesser, M. A., Socia, Q., Wysocki, P. A., Yenawine, M., & Shafter, A. W. 2018, *ATel*, **12181**, 1  
 Erdman, P., Darnley, M. J., Healy, M. W., Shafter, A. W., & Williams, S. C. 2022, *ATel*, **15802**, 1  
 Erdman, P., Kaur, A., Hartmann, D. H., et al. 2018, *ATel*, **11144**, 1  
 Ferland, G. J., Chatzikos, M., Guzmán, F., et al. 2017, *RMxAA*, **53**, 385  
 Förster, F., Cabrera-Vives, G., Castillo-Navarrete, E., et al. 2021, *AJ*, **161**, 242  
 Fukue, J. 2002, in *8th Asian-Pacific Regional Meeting*, Volume II, ed. S. Ikeuchi, J. Hearnshaw, & T. Hanawa (Tokyo: Astronomical Society of Japan), **325**  
 Galloway, D. K., Ackley, K., Wiersema, K., et al. 2020, *ATel*, **14141**, 1  
 Gehrels, N., Chincarini, G., Giommi, P., et al. 2004, *ApJ*, **611**, 1005  
 Gehrz, R. D., Truran, J. W., Williams, R. E., & Starrfield, S. 1998, *PASP*, **110**, 3  
 Ginsburg, A., Sipőcz, B. M., Brasseur, C. E., et al. 2019, *AJ*, **157**, 98  
 Hachisu, I., Kato, M., & Nomoto, K. 1996, *ApJL*, **470**, L97  
 Harris, C. R., Millman, K. J., van der Walt, S. J., et al. 2020, *Natur*, **585**, 357  
 Henze, M., Darnley, M. J., Kabashima, F., et al. 2015a, *A&A*, **582**, L8  
 Henze, M., Darnley, M. J., Shafter, A. W., et al. 2015b, *ATel*, **7984**, 1  
 Henze, M., Darnley, M. J., Shafter, A. W., et al. 2016a, *ATel*, **9853**, 1  
 Henze, M., Darnley, M. J., Shafter, A. W., et al. 2016b, *ATel*, **9872**, 1  
 Henze, M., Darnley, M. J., Shafter, A. W., et al. 2018a, *ATel*, **12182**, 1  
 Henze, M., Darnley, M. J., Shafter, A. W., et al. 2018b, *ATel*, **11121**, 1  
 Henze, M., Darnley, M. J., Shafter, A. W., et al. 2018c, *ATel*, **11130**, 1  
 Henze, M., Darnley, M. J., Shafter, A. W., et al. 2018d, *ATel*, **12207**, 1  
 Henze, M., Darnley, M. J., Williams, S. C., et al. 2018e, *ApJ*, **857**, 68  
 Henze, M., Ness, J. U., Darnley, M. J., et al. 2014a, *A&A*, **563**, L8  
 Henze, M., Ness, J.-U., Darnley, M. J., et al. 2015c, *A&A*, **580**, A46  
 Henze, M., Pietsch, W., Haberl, F., et al. 2010, *A&A*, **523**, A89  
 Henze, M., Pietsch, W., Haberl, F., et al. 2011, *A&A*, **533**, A52  
 Henze, M., Pietsch, W., Haberl, F., et al. 2014b, *A&A*, **563**, A2  
 Hernanz, M., & Jose, J. 1998, in *ASP Conf. Ser.* 137, *Wild Stars in the Old West*, ed. S. Howell, E. Kuulkers, & C. Woodward (San Francisco, CA: ASP), **368**  
 Hillman, Y., Prialnik, D., Kovetz, A., & Shara, M. M. 2016, *ApJ*, **819**, 168  
 Hornoch, K., Kucakova, H., Henze, M., et al. 2018, *ATel*, **11124**, 1  
 Hornoch, K., Kucakova, H., Wolf, M., et al. 2019, *ATel*, **13279**, 1  
 Horst, J. C., Abreu, B. M., Amiri, M. I., et al. 2019, *ATel*, **13281**, 1  
 Hunter, J. D. 2007, *CSE*, **9**, 90  
 Iijima, T., & Esenoglu, H. H. 2003, *A&A*, **404**, 997  
 Itagaki, K., Gao, X., Darnley, M. J., et al. 2016, *ATel*, **9848**, 1  
 Itagaki, K., Vanmunster, T., Watanabe, F., et al. 2021, *ATel*, **15034**, 1  
 Jester, S., Schneider, D. P., Richards, G. T., et al. 2005, *AJ*, **130**, 873  
 K., I. 2016, Central Bureau for Astronomical Telegrams, "Transient Object Followup Reports", <http://www.cbata.harvard.edu/unconf/followups/J00452885+4154094.html>  
 Kato, M., & Hachisu, I. 1994, *ApJ*, **437**, 802  
 Kato, M., & Hachisu, I. 2003, *ApJL*, **587**, L39  
 Kato, M., Saio, H., & Hachisu, I. 2015, *ApJ*, **808**, 52  
 Kato, M., Saio, H., Hachisu, I., & Nomoto, K. 2014, *ApJ*, **793**, 136  
 Kato, T., Nakajima, K., Maehara, H., & Kiyota, S. 2009, arXiv:0904.2228  
 Kaur, A., Hartmann, D. H., Gonzalez, G., et al. 2018a, *ATel*, **11134**, 1  
 Kaur, A., Hartmann, D. H., Henze, M., Shafter, A., & Darnley, M. 2018b, *ATel*, **11125**, 1  
 Kaur, A., Hartmann, D. H., Henze, M., Shafter, A., & Darnley, M. J. 2018c, *ATel*, **11126**, 1  
 Kaur, A., Rajagopal, M., Hartmann, D. H., et al. 2018d, *ATel*, **12205**, 1  
 Kaur, A., Rajagopal, M., Hartmann, D. H., et al. 2019, *ATel*, **13302**, 1  
 Knigge, C., Toonen, S., & Boekholt, T. C. N. 2022, *MNRAS*, **514**, 1895  
 Korotkiy, S., & Elenin, L. 2011, Central Bureau for Astronomical Telegrams, "Transient Object Followup Reports", <http://www.cbata.harvard.edu/unconf/followups/J00452885+4154094.html>  
 Kumar, H., Bhalerao, V., Anupama, G. C., et al. 2022, *AJ*, **164**, 90  
 McKinney, W. 2010, in *Proc. 9th Python in Science Conf.* 445, ed. S. van der Walt & J. Millman, 51  
 McLoughlin, D., Blundell, K. M., Lee, S., & McCowage, C. 2021a, *MNRAS*, **503**, 704  
 McLoughlin, D., Blundell, K. M., Lee, S., & McCowage, C. 2021b, *MNRAS*, **505**, 2518  
 Mondal, A., Das, R., Anupama, G. C., & Mondal, S. 2020, *MNRAS*, **492**, 2326  
 Munari, U., Giroletti, M., Marcote, B., et al. 2022, *A&A*, **666**, L6



- Naito, H., Kiyota, S., Sano, Y., et al. 2021, *ATel*, **15068**, 1
- Naito, H., Watanabe, F., Sano, Y., et al. 2018, *ATel*, **11133**, 1
- Nasa High Energy Astrophysics Science Archive Research Center (Heasarc) 2014, HEASoft: Unified Release of FTOOLS and XANADU, Astrophysics Source Code Library, ascl:1408.004
- Ness, J. U., Drake, J. J., Beardmore, A. P., et al. 2009, *AJ*, **137**, 4160
- Nishiyama, K., & Kabashima, F. 2008, Central Bureau for Astronomical Telegrams, M31 (Apparent) Novae Page, 2008-12a, [http://www.cbat.eps.harvard.edu/iau/CBAT\\_M31.html#2008-12a](http://www.cbat.eps.harvard.edu/iau/CBAT_M31.html#2008-12a)
- Nishiyama, K., & Kabashima, F. 2012, Central Bureau for Astronomical Telegrams “Transient Object Followup Reports”, <http://www.cbat.eps.harvard.edu/unconf/followups/J00452884+4154095.html>
- Nomoto, K., Saio, H., Kato, M., & Hachisu, I. 2007, *ApJ*, **663**, 1269
- O’Brien, T. J., Bode, M. F., Porcas, R. W., et al. 2006, *Natur*, **442**, 279
- Ogilvie, G. I., & Livio, M. 2001, *ApJ*, **553**, 158
- Oksanen, A., Darnley, M. J., Shafter, A. W., et al. 2019, *ATel*, **13269**, 1
- Page, K. L., Kuin, N. P. M., & Osborne, J. P. 2022, *Univ*, **8**, 643
- Pavana, M. 2020, PhD thesis, Pondicherry Univ.
- Pavana, M., Anche, R. M., Anupama, G. C., Ramaprakash, A. N., & Selvakumar, G. 2019, *A&A*, **622**, A126
- Pavana, M., Kiran, B. S., Sujith, D. S., & Anupama, G. C. 2018, *ATel*, **12195**, 1
- Pedregosa, F., Varoquaux, G., Gramfort, A., et al. 2011, *JMLR*, **12**, 2825
- Perez-Fourmon, I., Alarcon, M. R., Barrios-Perez, J., et al. 2020, *ATel*, **14131**, 1
- Perez-Fourmon, I., Poidevin, F., Aznar Menargues, G., et al. 2022, *ATel*, **15786**, 1
- Perez-Fourmon, I., Poidevin, F., Reyes-Rodriguez, E., et al. 2023, *ATel*, **16370**, 1
- Poole, T. S., Breeveld, A. A., Page, M. J., et al. 2008, *MNRAS*, **383**, 627
- Postma, J. E., & Leahy, D. 2017, *PASP*, **129**, 115002
- Postma, J. E., & Leahy, D. 2021, *JApA*, **42**, 30
- Prialnik, D., & Kovetz, A. 1995, *ApJ*, **445**, 789
- Rajagopal, M., Rutherford, T., Henson, G., et al. 2020, *ATel*, **14158**, 1
- Ribeiro, V. A. R. M., Bode, M. F., Darnley, M. J., et al. 2009, *ApJ*, **703**, 1955
- Rodriguez, E. R., Menargues, G. A., Calatayud-Borras, Y., et al. 2023, *ATel*, **15902**, 1
- Rupen, M. P., Mioduszewski, A. J., & Sokoloski, J. L. 2008, *ApJ*, **688**, 559
- Schaefer, B. E. 2010, *yCat*, [J/ApJS/187/275](http://www.ycat.org/yCat/JApJS/187/275)
- Shafter, A. W., Adurkar, A., Bautista, V., et al. 2023, *ATel*, **16362**, 1
- Shafter, A. W., Burris, W. A., Horst, J. C., et al. 2022, *ATel*, **15797**, 1
- Shafter, A. W., Hornoch, K., Ciardullo, J. V. R., Darnley, M. J., & Bode, M. F. 2012, *ATel*, **4503**, 1
- Shore, S. N., Kenyon, S. J., Starrfield, S., & Sonneborn, G. 1996, *ApJ*, **456**, 717
- Singh, K. P., Stewart, G. C., Westergaard, N. J., et al. 2017, *JApA*, **38**, 29
- Singh, K. P., Tandon, S. N., Agrawal, P. C., et al. 2014, *Proc. SPIE*, **9144**, 91441S
- Socia, Q., Horst, J., Shafter, A. W., & Henze, M. 2018, *ATel*, **11118**, 1
- Sokoloski, J. L., Rupen, M. P., & Mioduszewski, A. J. 2008, *ApJL*, **685**, L137
- Sonith, L. S., Basu, J., Anupama, G. C., et al. 2021, *ATel*, **15045**, 1
- Starrfield, S. 1999, *PhR*, **311**, 371
- Starrfield, S. 2017, in *Evolution of Accreting White Dwarfs to the Thermonuclear Runaway*, ed. A. W. Alsabti & P. Murdin (Berlin: Springer), **1211**
- Steffen, W., Koning, N., Wenger, S., Morisset, C., & Magnor, M. 2011, *IEEE Trans. Vis. Comput. Graph.*, **17**, 454
- Strope, R. J., Schaefer, B. E., & Henden, A. A. 2010, *AJ*, **140**, 34
- Sun, G., Xu, J., Zhang, M., et al. 2023, *ATel*, **16361**, 1
- Taguchi, K., Kawabata, M., Isogai, K., et al. 2021, *ATel*, **15039**, 1
- Tan, H., & Gao, X. 2018, *ATel*, **12200**, 1
- Tan, H., Zhang, M., Zhao, J., et al. 2021, *ATel*, **15037**, 1
- Tan, H., Zhao, J., Zhang, M., et al. 2022, *ATel*, **15795**, 1
- Tandon, S. N., Postma, J., Joseph, P., et al. 2020, *AJ*, **159**, 158
- Tang, S., Bildsten, L., Wolf, W. M., et al. 2014, *ApJ*, **786**, 61
- Tang, S., Cao, Y., & Kasliwal, M. M. 2013, *ATel*, **5607**, 1
- Tody, D. 1993, in *ASP Conf. Ser. 52, Astronomical Data Analysis Software and Systems II*, ed. R. J. Hanisch, R. J. V. Brissenden, & J. Barnes (San Francisco, CA: ASP), **173**
- Van Rossum, G., & Drake, F. L. 2009, *Python 3 Reference Manual* (Scotts Valley, CA: CreateSpace), <https://www.python.org/>
- Virtanen, P., Gommers, R., Oliphant, T. E., et al. 2020, *NatMe*, **17**, 261
- Wagner, R. M., Woodward, C. E., Starrfield, S., Rothberg, B., & Kuhn, O. 2021, *ATel*, **15036**, 1
- Wang, B. 2018, *RAA*, **18**, 049
- White, N. E., Giommi, P., Heise, J., Angelini, L., & Fantasia, S. 1995, *ApJL*, **445**, L125
- Williams, B. F., Garcia, M. R., Kong, A. K. H., et al. 2004, *ApJ*, **609**, 735
- Wilms, J., Allen, A., & McCray, R. 2000, *ApJ*, **542**, 914
- Wolf, W. M., Bildsten, L., Brooks, J., & Paxton, B. 2013, *ApJ*, **777**, 136
- Wysocki, P. A., Socia, Q., Engesser, M. A., et al. 2018, *ATel*, **12190**, 1